Corlett, Hilary, Hodgetts, David, Hirani, Jesal, Rotevatn, Atle, Taylor, Rochelle and Hollis, Cathy (2021) A geocellular modelling workflow for partially dolomitized remobilized carbonates: an example from the Hammam Faraun Fault block, Gulf of Suez, Egypt. Marine and Petroleum Geology, 126. 104831 ISSN 0264-8172

DOI: https://doi.org/10.1016/j.marpetgeo.2020.104831

Publisher: Elsevier BV

Version: Accepted Version

A geocelluar modelling workflow for partially dolomitized remobilized carbonates: an example from the Hammam Faraun Fault Block, Gulf of Suez, Egypt

Hilary Corlett[1], David Hodgetts[2], Jesal Hirani[3], Atle Rotevatn[4], Rochelle Taylor[2], and Cathy Hollis[2]

[1]Earth and Planetary Sciences, MacEwan University, 10700 104 Ave NW, Edmonton, Alberta, Canada

[2]School of Natural Sciences, Williamson Building, Oxford Road University of Manchester, M13 9PL, UK

[3]X-ray Mineral Services, 1 Claughton Rd., Conwy, LL29 7EF, UK

[4]Department of Earth Science, University of Bergen, P.O. Box 7803, Bergen, N-5020, Norway

ABSTRACT

Constructing geocellular models of carbonate rocks using standard software is challenging since most of modelling packages are designed, first and foremost, to represent siliciclastic depositional systems, where rock properties are strongly facies-controlled. The distribution and components of carbonate depositional facies vary drastically across the geological timescale as a result of paleoclimate and its effects on carbonate-producing biota. Furthermore, reservoir architecture is less strongly controlled by depositional environment than in clastic settings, and rock physical properties, including fracture networks, are controlled by both primary components and their subsequent diagenetic alteration. This means that rock property distribution is less predictable than in siliciclastic systems, and less well represented by geocellular models that are designed to represent sedimentary architecture. In other words, in carbonate systems, the depositional and diagenetic history needs to be reconstructed in order to successfully model reservoir properties.

In this study a geocellular model was created by using a well-characterised outcrop analogue obtained from the Hammam Faraun Fault (HFF) Block, located on the eastern coast of the Gulf of Suez in Sinai, Egypt. This model integrates sedimentological, petrophysical, diagenetic, and structural information into a single database. The workflow utilizes the regional tectonic history, upscaled lithological logs, and two-stage facies modelling (reflecting in and ex situ depositional facies) and resulted in the creation a realistic model of remobilized carbonates that were deposited on the slope of a carbonate platform during a period of tectonic instability. Diagenetic overprinting was achieved using probability functions to reflect the history of burial, rifting, and the spatial relationship of stratabound and non-stratabound dolostone bodies. The study demonstrates a workflow for modelling mass-transport carbonate facies and multistage fault-related diagenesis so that flow controlling facies and diagenetically altered poroperm and fracture networks are accurately represented using commercially available modelling software, and in particular demonstrates how diagenetically controlled geobodies can be captured using simple algorithms.

1. Introduction

Although 3D geocellular-models have now been used for decades to reconstruct subsurface geological systems for the quantification of in place hydrocarbon reservoirs and well-planning, workflows have largely been driven by the need to represent the morphology and connectivity of flow-controlling bodies in siliciclastic systems. This in part reflects a better knowledge of the shape, size and morphology of sedimentary bodies in siliciclastic systems, from modern and ancient analogues (Jung and Aigner, 2012; Burchette, 2012). It is also commensurate with sedimentary facies offering a stronger influence on fluid flow in siliciclastic reservoirs. In carbonate reservoirs, there is significantly less data available to describe sedimentary body geometry. Carbonate reservoirs are heterogeneous and complex, owing to the changes in depositional systems through determined by what components of the carbonate factory are present or absent (Pomar and Hallock, 2008) and diagenetic overprinting, which influence the physical rock properties of carbonate faciesand fracture abundance (Sharp et al., 2006; Pöppelreiter et al., 2008; Pyrcz and Deutsch, 2014). In deep-water carbonate systems, further complexity is introduced by the sparse database of mass carbonate transport facies may be due to lack of study, and almost certainly to the difficulty associated with prediction, imaging, and modelling complex carbonate facies in outcrop and in seismic – i.e. facies boundaries are often more transitional – and the strong stratigraphic control on body geometry

A second complexity in carbonate systems is that porosity and permeability are usually not just controlled by sedimentary facies, but also by diagenetic and structural modification. In particular, dolomitization, dissolution, cementation, physical and chemical compaction (Humprey et al., 2020), and fracturing can strongly influence how fluids flow. Consequently, construction of reservoir models requires that petrophysical properties are distributed in such a way that post-depositional modification of the pore structure is accounted for alongside primary, sedimentary features. This is a grand challenge of carbonate reservoir modelling and has been approached in many different ways, including 1) modification of model properties to account for observed patterns of fluid flow (e.g. by use of permeability multipliers, or modification of K_v/K_h) (Gomes et al., 2018), 2) petrophysical rock typing (Hollis et al., 2010; Skalinski and Kenter, 2014; Ghadami et al., 2015; Fu et al., 2018) or 3) building diagenetic overlays and/or fracture overlays to merge with the sedimentological model of rock properties (Pöppelreiter et al., 2008; Sharp et al., 2010). Option 1 is efficient and might permit history mapping, but has no geological constraint and therefore could lead to inaccurate forecasting. Option 2 utilises petrophysical and geological data, ideally alongside production data, but can be time consuming and it may be difficult to extrapolate the rock types predictively between wells. Option 3 is geologically robust, and improves our understanding of the impacts associated with depositional, diagenetic, and structural aspects of a carbonate reservoir but can increase both model construction and run times, and may be difficult to construct with minimal input data.

Finally, scale is a real problem in carbonate systems. Carbonate pore networks are difficult to characterize due to the variability of carbonate grain types and size (controlled by the composition of the carbonate factory), the heterogeneity of the depositional environment, and multiple phases of diagenesis, which can create multi-modal pore systems. Conventional measurement of porosity and permeability is usually conducted on core plugs that are ~2.5 cm diameter, but it is not unusual for pores to be 1 cm or more in diameter (e.g. fossil and clast molds), meaning that core plugs cannot reasonably measure total porosity and permeability (Sharp et al., 2010). Furthermore, fractures are present in nearly all carbonate systems, and often control flow but it is notoriously difficult to measure fracture permeability, particularly in the absence of well data and at different scales (Koehrer et al., 2010).

In totality, carbonate depositional facies, diagenesis, and fracture networks are all heavily influenced by sedimentological processes and the tectonic evolution of the basin in which they were deposited (Pöppelreiter et al., 2008). Although this statement is widely accepted to be true, it is not common to find modelling workflows that directly acknowledge the importance of basin evolution on sedimentary and reservoir architecture; ie. there is often a disconnect between geological knowledge and model construction. A key objective of this study was to build a 3D geocellular model that represented the shape, size and distribution of flow controlling geobodies on the Hammam Faraun Fault (HFF) Block by incorporating knowledge of each step of the region's geological history, from pre-rift sedimentation to syn-rift dolomitization and fracturing. The aim of the model was to integrate spatial sedimentological, structural, diagenetic and petrophysical data into a single database and extrapolate 2D and pseudo-3D facies data fully into a 3D visualisation. As part of this process, it was necessary to determine a method by which both depositional geobodies and diagenetic overprinting could be represented in 3D space. Reservoir modelling packages have largely been formulated to model siliciclastic reservoirs, and therefore many of the default algorithms are not directly applicable to carbonate systems. Although advances are now being made in carbonate reservoir modelling, these often rely on bespoke geostatistical modelling (e.g., Beucher and Renard, 2016), prior outcrop data in order to constrain models, for example using multipoint statistics (e.g., Janson and Madriz, 2012), specifically consider only one element of the reservoir, such as fractures (e.g., Geiger and Matthai, 2014) or focus on cyclicity rather than discontinuous sedimentary or diagenetic geobodies (e.g., Le Blevec et al., 2020). In particular, there are few published examples of geocellular models that aim to reproduce the spatial distribution and morphology of diagenetic geobodies using commercial software (Pöppelreiter et al., 2008; Gomes et al., 2018).

The reservoir model presented in this study therefore provides a workflow for modelling carbonate facies within a mass-transport facies complex, as well as stratabound and non-stratabound dolostone bodies. This requires that it captures the spatial distribution of both discontinuous sedimentary bodies and diagenetic geobodies. Although the model is based on measured geobody size, and mapped geobody distribution in outcrop, the workflow may be used to produce subsurface models, where the direct measurement of carbonate facies dimensions, diagenetic geobodies, and fractures is not possible, or where there is limited spatial data, but where there is prior knowledge of basin evolution. It also contributes to a growing database of remobilised carbonate facies dimensions and their associated petrophysical properties prior to and post diagenetic overprinting.

2. Geological Setting

2.1. Structure

The HFF Block is located along the eastern coast of the Gulf of Suez, north of Abu Zenima, on the Sinai Peninsula (Fig. 1). Prior to rifting and formation of the Gulf of Suez, the Arabo-Nubian massif experienced compressional tectonism due to the convergence of the African and Eurasian plates and closure of the Neotethys, starting in the Late Cretaceous

(Bosworth et al., 1999). The area that was created by this compression is known as the Syrian Arc Fold Belt (SAFB) or the ‘unstable shelf’, while the ‘stable shelf’ in southern Sinai and Jordan, remained largely unaffected (Bosworth et al., 1999; Youssef, 2003). During closure of the Neotethys, anticlinal ridges formed where Permian faults were reactivated along the unstable shelf. These acted as platforms for shallow-water carbonate deposition whilst between them, deeper water deposits accumulated (Moustafa and Khalil, 1995; Youssef, 2003; Spence and Finch, 2014). Deposition in these basins began in the Cretaceous and continued until the early Tertiary (Sharp et al., 2000). The Gulf of Suez developed in the Late Oligocene when the African Plate separated from the Arabian Plate (23 Ma), as an extension of the Red Sea (Patton et al., 1994; Gawthorpe et al., 2003; Jackson et al., 2006) and continued into the Miocene (Bosworth et al., 2012). The rift is divided into three mega blocks each with its own characteristic dip direction, and each block is bound on one side by a major listric normal fault and the other by a normal fault with minor throw (Mustafa and Abdeen, 1992). The grabens that comprise these provinces include the Hammam Faraun block, which is bound on its western edge by the HFF (Robson, 1971).

2.2. Stratigraphy

The stratigraphic succession in Sinai is divided into three megasequences; two are considered pre-rift, and one post-rift (Fig. 1). The first megasequence comprises dominantly non-marine siliciclastics that directly overlie the Precambrian basement rocks. These strata are known collectively as the Nubian sandstones. Their depositional extent stretches from Northern Africa into the Middle East and they were deposited from the Cambrian to the Late Cretaceous (Jackson et al., 2006). Megasequence two is a Mesozoic to Tertiary age succession and was deposited prior to rifting when the SAFB was active. One of the anticlinal ridges associated with the SAFB that developed in the unstable area of the Arabo-Nubian massif formed through reactivation of the Wadi Araba fault. Repeated tectonism along the Wadi Araba fault during deposition of the Thebes Formation led to multiple stacked mass-transport deposits in the HFF Block study area (Corlett et al., 2018). Finally, the third syn-rift megasequence unconformably overlies the earlier pre-rift strata comprising siliciclastics of the Nukhul Formation, overlain by evaporites of the Ras Malaab Group (Sharp et al., 2000).

2.3. Depositional Environment – Thebes Formation

Throughout much of Sinai, the Thebes Formation comprises a lower mudstone layer with chert bands, a middle chalky limestone layer, and an upper chalky limestone with chert bands grading into a marly limestone in the uppermost strata (Moustafa and Abdeen, 1992). Reactivation of the Wadi Araba fault during the SAFB resulted in the deposition of mass-transport deposits south of Wadi Araba in the Galala Plateau region of the Eastern Desert (Scheibner et al., 2003; Höntzsch et al., 2011) and in the HFF Block study area along a NNW to SSE shallowly dipping ramp. The Thebes Formation at the HFF Block study site contains multiple mass-transport deposits that were deposited onto a middle to outer carbonate ramp consisting of slope to basin packstones (S-1 and B-1) to mudstones (Corlett et al., 2018). Mass-transport facies (R-1 to R-6) represent a history of tectonic instability during the SAFB along the Wadi Araba fault, currently located on the western side of the Gulf of Suez, northwest of the HFF Block (Schütz 1994). Full descriptions of these facies and the depositional history may be found in Corlett et al. (2018) and are summarized in Table 1. The Thebes Formation in the HFF Block is informally divided into lower and upper units with the lower dominated by mostly R-1 matrix supported conglomerate debrites, with sharp irregular base and convex upper contact, surrounded and draped by *in situ* slope packstones (S-1), and R-2 tabular, graded foraminifera grainstone turbidites beds that, when present, follow facies facies R-1, and overlain by facies S-1. The upper Thebes is dominated by thick basin mud- to wackestones with intermittent R-5 foraminiferal grainstone high-density turbidites beds. The R-1 facies varies in down-dip length between 3 to 267 m, along-strike between 2-64 m, and are between 0.3-20 m thick. The R-2 facies are 2-50 m in down-dip length, up to 100 m along strike, and between 0.5-6 m thick. The intermittent R-5 facies in the upper Thebes are much larger in their areal extent, measuring between 57 to 940 meters in down-dip and along-strike length, and between 0.5-10 m thick.

2.4. Dolomitization

Dolomitization occurred on the HFF Block adjacent to the HFF and along debrite and turbidite beds (Sharp et al., 2010; Hirani et al., 2018a and b). Field mapping, trace element geochemistry, stable and strontium isotopes revealed that dolomitization occurred during two distinct events, associated with the rift evolution of the Gulf of Suez (Hollis et al., 2017). Stratabound dolomitization occurred first, during rift initiation, from partially evaporated Oligo–Miocene sea- water descending down active faults into the basal Nubian sandstone aquifer before ascending into the HFF and flowing away from the fault and reacting with debrites and turbidite beds (Hirani et al., 2018a). A second interval of dolomitization occurred during the rift climax, forming non-stratabound, dolostone bodies within the core and damage zone of the HFF. Convection of seawater along the HFF at this time resulted in multiple phases of dolomitization and recrystallization in the HFF footwall, lasting approximately 10 Myr (Hirani et al., 2018b; Benjakul et al., 2020). Stratabound dolostone bodies in the HFF are hosted within matrix-supported debrites (R-1) and grainstone turbidites (R-5). They are up to 15m thick and up to 300m in length and terminate 2.5 km away from the HFF (Hirani et al., 2018a). Non-stratabound dolostone bodies form as discrete pods within the damage zone of the HFF, are up to 500m wide and 80m thick and have thin tongues of stratabound dolostone on their outermost margin (Hirani et al., 2018b). The two episodes of dolomitization affected porosity and fracture spacing differently in non-stratabound and stratabound dolostones compared to their precursor limestones (see Korneva et al., 2018).

3. Methodology

3.1. Data Collection

Data for the model was collected in the field at the HFF Block study site. Thirty-four lithological logs (totalling 909.69m) were recorded in the field ranging from 3.3 to 93.2 m in thickness. Of these 34 logs, 24 were recorded by hand and measured directly on the face of the exposure. The remaining ten logs were recorded as “laser logs” using a laser range finder (TruPulse 200L) to measure sections in inaccessible cliff faces (Corlett et al., 2018). The laser logs were recorded during a third field season, following facies and structural mapping, along with detailed facies descriptions. The weathered profile, which easily differentiated between mass-transport versus authochthonous slope and basinal facies, was used to differentiate facies in laser logs within the upper and lower Thebes. In the lower Thebes, the presence of absence of clasts and shape of the mass-transport facies (convex versus tabular upper contact, differentiated R-1 from R-2 facies. These logs were corrected for true dip and used alongside the directly measured sedimentological logs as inputs in the HFF Block model. A total of 400 samples were collected from the HFF Block, including a sample from each unit recorded in the 24 lithological logs that were by hand. Each sample was classified as one of seven facies defined in the HFF Block (Corlett et al., 2018) and used to populate and inform the distribution of facies within the HFF Block. Samples that had been dolomitized in the HFF Block were input to the model as their original depositional facies. In areas that were pervasively dolomitized, there remained sufficient remnant textural components (e.g., allochem or clast molds) to decipher the original depositional texture (Hirani et al., 2018a; 2018b).

3.2. Petrophysical Analysis

A total of 141, 25 mm diameter cores ranging in length between 13.97-74.49 mm were tested. 112 of these were used to measure porosity and permeability. Representative samples from facies D1, D3, D4, R1, and B1 were analysed under hydrostatic conditions to yield results at pressures equivalent to reservoir depths (up to 100MPa, equivalent to 3km overburden pressure). Samples that were collected in the field as intact blocks were cored using a diamond-tipped tool in a drill press adapted for wet coring. Each core was oven-dried at 60 °C for at least one week to remove intergranular water within the sample. After drying, cores were weighed (to within +0.002 g), and their dimensions measured using a digital calliper to +/-0.01 mm. From these measurements the dry density was calculated. All cores were stored in a sealed desiccation chamber with silica gel to prevent moisture re-entering the sample. Porosity was determined from grain volume and sample weight by helium injection using a ResLabTM DHP-100 digital helium porosimeter. Permeability was measured using a ResLabTM DGP-200 digital gas permeameter, calibrated for nitrogen gas use, and calculated using Darcy's Law. Each sample was measured three times to ensure that they were replicable, with an average value reported.

3.3. Input data and gridding

The geocellular model was constructed using Schlumberger Petrel^{TM} software with the following model inputs: lithological logs (Fig. 2A), digitized field photos and satellite imagery, field measurements, and laboratory determined petrophysical data (Korneva et al., 2018). The base model was created using digital elevation data that was extracted from Google Earth. The model grid was created using corner point gridding with faults serving as grid boundaries where present.

Faults were traced from Quickbird and Google Earth images and field observations, as well as mapped fault traces from published literature (Sharp et al., 2000; Young et al., 2003). Four faults were included in the model: the HFF, the Gebel Fault, the extension of the Gebel

Fault and the Thal Ridge Fault (Fig. 2B). Major stratigraphic breaks (formal and informal), defined in the model as ‘surfaces’, were created by digitizing Quickbird and Google Earth images that were supplemented by field photographs. The ‘make horizon’ process divided the grid into five major stratigraphic zones (Fig. 2C) using key surfaces (Upper Thebes Formation; Lower Thebes Formation; Esna; Sudr; Matulla). To capture the heterogeneity observed in the field, whilst maintaining a fit-for-purpose model, an aerial cell size of 25m x 25m was used. The upper Thebes and lower Thebes Formation were subsequently divided into 150 layers each while the Esna, Sudr and Matulla formations were not progressed in the modelling process, as our study was focused on the Thebes Formation, and dolomitization of the HFF Block. There were no dolomites encountered in the Esna, Sudr, or Matulla formations. The large number of layers were incorporated into the model to bring the vertical resolution to 1m, considered necessary to capture small-scale vertical facies heterogeneity. All the layers in this project were modelled as conformable, after petrographic and field examination of contacts revealed no evidence for extended periods of non-deposition and emplacement of remobilized facies, driven by tectonism, appears to have been contemporaneous with deposition on the slope (Corlett et al., 2018).

3.4. Upscaling

Prior to facies modelling, the sedimentogical logs inserted into the model as pseudo-well logs, where depths were converted to x, y, and z positions using differential GPS co-ordinates. The pseudo-well logs were upscaled using an averaging process that transfers measured rock properties represented in continuous logs into the grid. Facies from thirty-four pseudo-wells were upscaled utilizing a ‘most of’ averaging method that selects the facies that occurs with the highest frequency in each cell, to honour the facies recorded in the sedimentary logs.

3.5. Facies model

Pixel-based techniques and object modelling were both tested to determine the geostatistical method to construct a facies model that best matched field observations. Pixel-based modelling was performed using Petrel^{TM}’s Sequential Indicator Simulation (SIS) that uses variograms to represent the size, shape and distribution of the facies (Koehrer et al., 2010). The inputs for the SIS variograms were derived from the measurements of carbonate facies in the field and digital image analysis (Table 1). Petrel^{TM}'s Stochastic Object Modelling was also tested in facies modelling, to determine which of the two methods produces mass transport geobodies that more closely resemble those observed in the field. In this method, the general shape of the geobody is chosen (i.e., fan, lobe, channel) and the dimensions of the body are input as a range, in this case, defined by the range of facies dimensions measured in the field. Facies modelling was divided into two key stages: (1) autochthonous depositional carbonate facies modelling, followed by (2) allocthonous facies modelling. Facies proportions, defined from stratigraphic logs, were 26.9% for the facies B-1 and 26.1% for facies S-1 (both autochthonous facies), whereas authochthonous facies comprised ~40%. The allochthonous facies within the Thebes Formation were modelled using the pseudo-wells as seed points for facies distribution and their size and shape were modelled first using SIS. This variogram-based approach was used to model the S-1 facies (lower Thebes Fm) and facies B-1 (upper Thebes Fm) was used because they are ubiquitous across the field area, with poorly defined dimensions. These facies were defined as 'background facies'; essentially the template carbonate slope on which allochthonous facies with specific geometries could be object modelled.

Allochthonous deposits were then modelled using two different stochastic-based modelling methods (Fig. 3):

a) with SIS informed by variograms that integrated the aspect ratio and azimuth of geobodies derived from digital image analysis of facies R1-R6 (Figs. 3 and 4; Table 1). In this method, lithologies were interpolated between upscaled field and laser logs, where there was evidence of connectivity on the basis of field photos, and a NNE-SSW direction of flow measured in remobilised facies in the field, was used to steer geobody alignment and distribution.

b) using object-based modelling to distribute allochthonous facies based on field-determined geobody size and continuity, as well as a NNE-SSW direction of flow. This method honoured the variability in the shape and size of the remobilised geobodies observed in the field using specific, facies-based rules. Specifically, geobody dimensions were extracted from digital analysis of field photographs and satellite images (Fig. 4; see Corlett et al. 2018 for methodology) and these data were used to design object-based modelling algorithms. For example, the matrix-supported debrites (R-1) were considered best represented by a half-ellipse with a rounded top, whilst grainstone turbidite facies (R-2) were given a fan/lobe shape (Fig. 3).

The two facies models were compared quantitatively using percent proportions of each facies from the well logs and comparing to upscaled and modelled proportions and qualitatively by comparing the morphology and connectivity of facies compared to digital image analysis of field photographs as well as field measurements.

3.6. Dolostone model

Once visual assessment showed that the facies model was considered to closely resemble the HFF Block study area, by comparison with a) field photos, b) modelled facies volumes and distribution compared to field logs, and c percent proportions of each modelled facies to the percent proportion of the sedimentary logs, the second phase of modelling focussed upon construction of the stratabound and non-stratabound dolostone bodies. Stratabound dolostone bodies, hosted within matrix-supported debrites (R-1) and grainstone turbidites (R-5), terminate 2.5 km away from the HFF (Hirani et al., 2018a). Non-stratabound dolostone were mapped as up to 500m wide and 80m thick. The non-stratabound dolostone pods have stratabound dolomites terminations (Hirani et al., 2018b), but these are much smaller than the first phase stratabound dolomites and only extend away from these massive dolomite bodies up to a few tens of meters.

Two hypotheses were considered for the formation of the dolostone bodies. The first (Hypothesis A) considered that the two main body types are genetically related and formed by the upwards flux of fluids along the HFF, followed by selective dolomitization of the highest permeability beds at >500m from the fault (Sharp et al., 2010; Yao et al., 2020). Hypothesis B considered the stratabound dolostone bodies to have formed first, followed by overprinting by the formation of the non-stratabound dolostone in proximity to the HFF. A key conclusion of this study is that Hypothesis B is the preferred conceptual model (Hollis et al., 2017), but the geocellular models for both hypotheses are presented here for completeness.

Hypothesis A reflects the base case hypothesis for this study (Sharp et al., 2010) and considers dolomitization on the HFF Block to represent a ‘Christmas Tree’ type geobody formed by hydrothermal fluids. In order to capture this hypothesis, and thereby model the distribution of dolostone, two probability density functions were used to distribute the dolostone, with supporting ‘if’ statements. For the stratabound dolostone bodies, the probability of dolomitization occurring in the lower Thebes in matrix supported debrites (R-1) and grainstone turbidites (R-2) was set to 1, with all other facies being set to 0. This probability function was integrated with a statement that dolomitization could occur for up to 2.5 km from the HFF, with a decreasing probability of dolomitization with increasing distance (Fig. 5). This particular dimension was used, after testing a series of measurements, because it resulted in termination of any stratabound dolomite bodies at the locations which they were observed in the field.

Not every R-1 debris flow in the lower Thebes Formation is dolomitized, so using a probability function to overprint or replace any R-1 facies within 2.5 km of the HFF fault with dolomite resulted in overestimation of the dolomite bodies. Two methods were employed to reflect the natural variability in the location and volume of dolomitized debris flows observed in the field. The first method, following Sharp et al. (2006) used a percentage to populate a certain volume of the R-1 facies. The percent dolomitized bodies were calculated from logs (23%); however, the results were found to underestimate the number of dolomitized R-1 facies, based on comparison with field photographs. The second method employed a random function, where the result of the probability dolomite modelling was multiplied by a random function (Fig. 5E). The random function, populated with probabilities of 0 to 1, was pixelated and would produce unnatural, patchy dolomite bodies. Instead, a smoothed random probability function was included to ensure that not every debrite geobody was dolomitised within 2.5 km from the HFF. This resulted in some of the debrite bodies being dolomitised, partially dolomitised, or unaltered, which accurately reflects observations of dolomitized bodies in the field.

For the non-stratabound dolostone body, the probability of dolomitization for all facies was set to 1 in proximity to the fault, decreasing to 0 at 1.25 km from the fault (Fig. 6) to constrain the body to the fault core, as seen in the field. The number 1.25 km was used in the probability after several (n=5) iterations to replicate the distribution that was observed in the field. In order to create a more realistic margin to the dolostone body, a normal distributed random value was used.

The preferred conceptual model to explain dolomitization on the HFF Block is that the stratabound dolostone bodies formed during the earliest syn-rift, and were then overprinted by non-stratabound dolomitization in the core of the HFF at rift climax (Hollis et al., 2017). To capture this conceptual model, a slightly different modelling approach was adopted. Firstly, the stratabound dolostone bodies were modelled using the dolostone probability function used for Hypothesis A (Fig. 4 A, C, D) and a smoothed random function was multiplied to the probability (Fig. 4E, F).

Once the stratabound dolostone bodies had been modelled, the non-stratabound dolostone bodies were distributed as discrete pods (north and south bodies; Fig. 6) using a localised point source. In this case, the diagenetic overprint was modelled as a halo around a fault stick emplaced into the model, based on field observations and dimensions of non-stratabound dolomite bodies. This represented a localised conduit (fracture) for dolomitising fluids associated with the HFF damage zone with the observed field dimensions of the bodies used to distribute the dolostone via a probability function away from the fault stick. To capture the stratabound dolostone associated with the non-stratabound dolostone bodies, a second probability function was added. The second probability function modelled a second dolostone 'facies' that over printed the original stratabound dolostones (Fig. 6).

3.7. Petrophysical model

Matrix petrophysical attributes were modelled separately from fracture-induced petrophysical properties. A Sequential Gaussian Simulation (SGS) algorithm (Deutsch and Journel, 1992) was used to model both porosity and permeability, which were conditioned to facies. Porosity was populated using a normal distribution while permeability was modelled as a lognormal distribution (Wantanabe et al., 2019). Minimum, maximum, mean and standard deviation statistics for every petrophysical property was derived and used to constrain the distribution of petrophysical properties instead of upscaled well attributes, because of the relative sparsity of data across the modelled area. Variograms were conditioned to the variance derived from each modelled facies, with sill and nugget set to 1 and half the calculated major, minor and vertical distances used to ensure intra-facies variability for each property.

3.8. Fracture model

The fracture model was built by generating a distinct stochastic fracture network for each facies (including two dolostone 'facies'). Each fracture network may have had more than one fracture set. Fracture orientations from scanline data collected in the field (Eker, 2013; Korneva et al., 2018) were converted to azimuth (strike + 90), and input as dip/azimuth data to Petrel. (Figs. 7 and 8)

3.8.1. Fracture intensity

Fracture intensity was input on a per facies basis using a P_{10} = number of fractures/length of scanlines = N/L*[L^{-1}] (Mauldon et al., 2000). P_{10} measures abundance in a specified orientation, and so is converted into a direction independent P_{32}, equivalent to fracture area per unit volume (P_{32}=$C_{31}P_{10}$; Mouldon et al., 2000; Wang *et al*., 2005). Consequently, the number of fractures measured in the field was dependent upon the orientation of the scanline, such that only fractures perpendicular to the scanline were sampled. The C_{31} function accounts for this (Terzaghi weighting factor; Wang et al., 2005) and was calculated by C_{31}=cosec(90-δ) or 1/cosδ where δ is the acute angle between the axis of the scanline and the resultant fracture pole (Fig. 9). As the resultant acute angle approaches 90^o, the correction factor approaches infinity, and therefore a maximum cut of correction of C_{31}=6 was applied. Where the angle δ is zero, the fracture pole and the axis of the scan line coincide, giving a correction of 1 (i.e. P_{32}=P_{10}). The dip and azimuth data for each facies was visualised in Petrel using a lower hemisphere stereonet plot, and then exported to calculate the Fisher K value, mean dip and azimuth for all fracture sets. The Fisher distribution required the fractures to be represented by their unit vectors, and was used to populate cells according to the calculated distribution and the P_{32} density value (Warden, 2014) (Fig. 10).

3.8.2. Fracture Length

No fracture lengths were available from field data, and therefore it was assumed that all fractures were mechanically constrained to bed thickness and an elongation ratio of 2:1 (horizontal length = 2*vertical length) was used (Table 2). A power law probability density function was used to reflect the probability of generating a fracture that is inversely related to the fracture length; i.e. it is less likely that longer fractures will be generated than shorter ones. The majority of fractures generated therefore tended towards the minimum length, leading to long processing times for the model. Consequently, the smaller fractures were modelled implicitly by using averaged permeability, dip, azimuth and aperture per cell (IFM model) whilst the larger fractures were modelled as a discrete fracture network (DFM) (Fig. 11). This was considered appropriate in this study, as the longer fractures appear to have controlled flow more than localised fractures, hence preserving flow direction during flow simulation. It also led to faster, more efficient run times. The maximum cut off for the IFM was set at half of the maximum fracture length.

3.8.3. Fracture aperture and permeability

There was only limited field data available to constrain fracture aperture, which is an unreliable measurement in outcrop because of uplift and weathering effects. A default mean aperture of 0.075mm was therefore used, using a log-normal distribution. These apertures were then related to permeability using a cubic law (Klimczak et al. 2010). Cubic law assumes laminar flow, and allows integration of the Navier Stokes equation and the Darcy equation (Hubbert 1957), permeability such that:

$$Q= - (PL-Pi)/L*KA/\mu = -(PL-Pi/L)*Kwa/\mu = (PL-Pi)/L*wa3/12\mu$$

Where Q is flow rate, PL-Pi is the pressure differential, K is permeability, A is area, a is aperture, w is width, L is length and μ is viscosity, such that:

$$K=a^2/12 = aperture/12 = 0.000075^2/12 * 4.6875 \text{ x } 10^{-10}m = 474960mD$$

In total, 14 fracture sets were created in the DFN, using the upscaled grid in order to maintain viable model run times. A sector of the permeability model is shown in Figure 12, for the massive dolomite body.

4. Results

4.1 Facies Model

An aerial cell size of 25m x 25m and 150 layers (1 layer = 1 m), representing the total thickness Thebes Formation, resulted in a model size of 2, 491, 145 cells. Two different facies models were created using upscaled sedimentary pseudo-well logs, one using SIS, and the other using object-based stochastic facies. Qualitative assessment of these two techniques to well logs and field photos favours the object-based modelling since the boundaries of these facies were known from field measurements, and are accurately represented by the object-based modelling (Fig. 13A). A quantitative comparison of the original and upscaled logs revealed that upscaling resulted in an overestimation of the R-1 debris flow facies (> 5%), but all other upscaled facies were predicted within 5%. Both the SIS and object-based facies modelling approaches resulted in similar values (within 5%) to the upscaled logs, with the exception of the B-1 wackestone facies, which estimates over 10% more of this autochthonous facies compared to the original and upscaled logs (Fig. 13B).

4.2 Dolomite Model

The results of modelling Hypothesis A resulted in a classic “Christmas tree” style of dolomitization where, in proximity of the fault, large non-stratabound dolomites that transition into stratabound dolomites that extend away from the fault. In Hypothesis B, the stratabound dolomites are emplaced first and then overprinted by a second non-stratabound phase that follows fracture conduits associated with the HFF footwall damaged zone (Fig. 14). Hypothesis A overestimates the degree of dolomitization observed in proximity to the HFF and did not allow for differentiation of petrophysical properties and fracture characteristics between different generations of dolomite (Hollis et al., 2017; Korneva et al., 2018). All of the petrophysical and fracture models were constructed using the model for Hypothesis B.

4.3 Fracture and Petrophysical Models

The porosity and the permeability models are shown in Figure 15 and comparison of the input and modelled data (Table 3) shows that although the mean values varied slightly between measured and modelled data, the standard deviation and range was consistent between input and output data.

The results of fracture modelling (Figs. 10-12) honour the trends observed in the field and on digital outcrop photographs, which showed that there was no clear relationship between fracture density and facies within the stratabound dolostone, but that there was a facies control on fracture spacing within the non-stratabound dolostone in the damage zone of the HFF (Korneva et al., 2018).

5. Discussion

5.1. Facies models

Comparison of volumetric statistics from both models show that they both apparently over-represent certain facies, in particular the background wackestone facies (Fig. 13). Nevertheless, the volume of mass-transport deposits is reasonably preserved by both SIS and object modelling methods. The size of the model included a large volume of the HFF Block that had not been logged sedimentologically, particularly within the Upper Thebes member but which had been mapped and viewed using satellite imagery. These data show that a greater proportion of mass-transport deposits were spatially restricted to the Lower Thebes member. By modelling the entire Thebes Formation, including areas which had been less well described sedimentologically, the volume of authocthonous facies in the upper Thebes was necessarily increased in the model compared to the input data.

Although both of the facies models created for this study honoured the log data of the remobilised facies to within 5% of the total proportion, visual comparison of the SIS model with digitized field photos and satellite images that were calibrated using direct field measurements indicated that it did not sufficiently capture geobody size and morphology (Fig. 4). In particular, the bodies do not reflect the upper convex geometry of the debrites, nor the slightly lobate geometry of the grainstone turbidite facies. This is not surprising, since mass-transport facies are not as laterally extensive as slope or basinal facies, and they generally travel as cohesive units resulting in lens or fan-shaped deposits that are not accurately represented by the variogram-based SIS modelling technique.

In comparison, the object-based model produced geobodies comparable to those geobody dimensions collected in the field. In particular, Facies R-1 debrites are much thicker, and less laterally extensive, than the other most common remobilised R-5 turbidite facies (Fig. 13B) and this is captured by the object-based facies model. In order to honour the proportion of each mass-transport facies, the SIS model includes more frequent, thinner facies when compared to the object-based facies model (e.g. Facies R-1 in Figure 13A). The object modelling also reflected the different dimensions of the debrites in the dip-parallel, versus perpendicular dimensions, since the object modelling allows for more precise shape descriptors. In totality, the object model reasonably matched the volume and distribution of facies, and on comparison with digital analysis of outcrop photos, better matched the shape and distribution of the facies as they were observed in the field.

When detailed geobody shape and dimensional data are not available, for example when building subsurface models, SIS could be considered an adequate representation of remobilised facies embedded in autochthonous facies. Borehole image logs and drill core data may be used to differentiate remobilized mass transport carbonate facies (Asmus and Grammer, 2013), but in most cases would only capture their thickness. Where outcrop data is available, variogram descriptors may be modified to reflect the shape and size of mass transport facies and their orientation if there is knowledge of the paleogeographic setting and transport direction (e.g., from paleocurrent data). In this study, confidence in the morphology, boundaries, size and distribution of mass transport facies from field data meant that object modelling could optimally reproduce the data collected in the field and using digital image analysis (Corlett et al., 2018).

5.2. Dolostone model

The dolostone model that was based on Hypothesis A reflected the concept of reactive fluid flux up and along faults and into the surrounding Thebes Formation. In this model, dolomitization took place principally in proximity to the HFF, to form a non-stratabound dolostone body, with continued reaction within distinct beds as fluids moved away from the fault to form stratabound dolostone. This created a geometry that was consistent with the conceptual model, but not with field observations. In particular, it created a thick, laterally extensive, non-stratabound dolostone body that extended along the plane of the HFF (Fig. 14 – Hypothesis A). Instead, field data shows that non-stratabound dolostone occurs in discrete pods within the damage zone of the HFF. These pods could have formed as a result of erosional truncation of the non-stratabound dolostone body, and therefore the geometry of the non-stratabound dolostone in outcrop could have been reproduced by truncation of its modelled form. However, field observations showed no evidence for such a process, with a distinct absence of non-stratabound dolostone along fault strike, away from the two bodies that were described by Hirani et al (2018b).

Secondly, the Hypothesis A model created a large number of stratabound dolostone bodies in close proximity to, and geometrically connected to, the non-stratabound dolostone body, consistent with the classic “Christmas tree” model of dolomitization (e.g., Beckert et al., 2015; Yao et al., 2020) Again, this is consistent with the conceptual model that fluids flowed away from the HFF, and reacted with specific, allochthonous, facies to form stratabound dolostone. Structural relationships and geochemical data unequivocally demonstrate, however, that stratabound dolostone bodies formed prior to the non-stratabound dolostone bodies from fluids that were vented from the proto-HFF (Hollis et al., 2017; Hirani et al., 2018a). Although stratabound dolostone bodies are observed, connected to the non-stratabound dolostone (so-called ‘dolostone-tongues’ of Hirani et al., 2018b), they are limited in lateral and vertical extent. Conversely, the Hypothesis A model results in formation of a large number of dolostone tongues that are connected to the non-stratabound dolostone body (Fig. 14 – Hypothesis A).

Taken together, this means that Hypothesis B is the preferred conceptual model since it best represents the conceptual geological model of fluid flow and reaction. Stratabound dolostone bodies are hosted within matrix-supported debrites (R-1) and grainstone turbidites (R-2) in the lower Thebes and are up to 15m thick, up to 300m in length and terminate 2.5km away from the HFF. In the model, the probability density function allows the dimensions and distribution, to be faithfully reproduced in three dimensions (Burnham and Hodgetts, 2019). The use of a probability density function permitted stratabound dolostone to be realistically populated within the model, tied to specific, allochthonous facies as observed in the field, which might be reasonably hypothesised in a subsurface model. Probability modelling also ensured localisation of the non-stratabound dolostone bodies at distinct points on the HFF, which had been identified in the field and interpreted to represent focused, vertical fluid flow at a point of structural complexity (a transfer zone) in the Suez Rift (Hollis et al., 2017). For this reason, even without field data, it would be feasible to model localised, non-stratabound dolostone at this location based on the predicted pattern of basin-scale fluid flow. For example, during exploration, when datasets are limited, a number of assumptions would need to be made and multiple realizations of the model using varying parameters run. In a data-rich field, with sufficient structural and diagenetic data, a more refined set of models could be built to capture dolomite body size, shape and rock properties in order to optimize reservoir development; for example, to target ‘sweet spots’ on the margins of dolostone bodies between zones of overdolomitization and dolostone – limestone contacts (Saller and Henderson, 1998; Sharp et al., 2010; Yapparova et al., 2017; Koeshidayaullah et al., 2020).

Finally, although the termination of the non-stratabound dolostone in the model was directly constrained by field data – which showed each body was < 500 m wide – the genetic relationship between the extent of dolomitization and the width of the fault damage zone (Hirani et al., 2018b) means that this body size could have been reasonably predicted from the structural model for the platform. There are numerous outcrop studies that document the size and shape of fault damaged zones and associated fracturing (e.g., Cianfarra and Salvini, 2016; Balsamo et al., 2019). In subsurface models it is difficult to be certain of fault damage zone geometries although the size may be estimated from width-to-throw ratios, at different stages of fault evolution (Ma et al., 2019). This means that if the width of the damage zone can be predicted, then methods outlined in this study can be used to model non-stratabound dolomite body size.

5.3. Rock property models

Analysis of the statistical variability in porosity and permeability by facies honoured the input data by retaining the highest permeabilities in grainstone turbidites and basinal wackestone facies, with lower porosity and permeability in dolostone, compared to limestone, facies (Fig. 15) (Korneva et al., 2018). Although these relationships seem counter-intuitive, they are consistent with measured porosity and permeability and reflect a) a high volume of solution-enhanced microporosity in the basinal wackestones and lime mudstones and b) pervasive ('over') dolomitization that resulted in occlusion of the intercrystalline pore network.

The results of fracture modelling (Figs. 10-12) were the most difficult to quality control because the input data was derived from a small number of local scan lines (n > 50). Despite a limited dataset, impacted by access restrictions to the field site during the latter stages of the study, it was possible to produce a model that reflected field observations. No relationship exists between fracture density and facies in stratabound dolomites but there is a facies control on fracture spacing in non-stratabound dolomites (Korneva et al., 2018). A particular challenge in the construction of the fracture model was determination of fracture length. Fractures are typically observed in only 1 or 2 dimensions in outcrop. Therefore, although scanlines allow an effective way of systematically collecting data on fracture orientation, present day aperture, fill and spacing, true fracture length is not observed because data is collected along a vertical face – essentially a cross-section (Bisdom et al., 2014). All scanlines were included in the model to reduce potential fracture orientation bias; however, truncation and censoring bias, in addition to the true fracture length bias associated with scanline sampling led to some uncertainty in the final fracture model. This uncertainty is further complicated when creating fracture models in the subsurface where well logs and drill cores allow a single scanline (Zeeb et al., 2013). In subsurface models, a deviated or horizontal log would result in more accurate fracture model inputs, but as in all subsurface models, the uncertainty would be much higher than in outcrop studies where fractures may be directly measured at various orientations. Where fractures can be observed on limestone pavements, then horizontal fracture length is more easily measured but the tip points of the fracture cannot often be observed and so vertical length cannot be determined. In essence, determination of the length, aperture and density of small fractures from field data carries a low level of confidence, and coupled with the long run times results in models that are potentially unstable. The more pragmatic approach was adopted in this study of modelling background fracture density to account for smaller, closely spaced fractures that will contribute to the overall permeability of the rock, therefore allows more scope to focus on the larger fractures, which in this study, have had a stronger influence on flow behaviour by creating a secondary pore network.

5.4. Simple but geologically realistic geocellular models

A challenge often faced by geoscientists is that they have to construct 3D reservoir models that represent a complex, multi-scale and multi-modal pore network in a short space of time, with incomplete data that might not be of an appropriate scale or extent. Often, the simplest approach is to average reservoir properties and create layer-based models, perhaps with reservoir property distribution guided by variograms. However, not only are many carbonate systems not truly layered, because of complex facies geometries and diagenetic overprint, there is also a real lack of data pertaining to the frequency of variance, with most studies focusing on dolomitized reservoirs (e.g. Jennings et al., 2000; Pranter et al., 2005; Budd et al., 2006).

In this paper, we propose a workflow that can easily be adopted to represent a layer-bound sedimentary sequence with stratabound diagenetic overprint tied to specific depositional elements. The facies model has been constructed using stochastic, pixel- and object-based methods calibrated to outcrop data. The stratabound diagenetic overprint is accounted for by training dolostone distribution to particular facies and distance from fault using a probability function. Such an approach has been successfully used in a few other subsurface studies (e.g. Warrlich et al., 2011; Lapponi et al., 2011). To account for the non-stratabound dolomitization, we have then superimposed a further diagenetic overlay using a discrete, object-modelling method. In a subsurface study, these bodies could be distributed deterministically, based on well and/or seismic evidence, or stochastically based on an interpreted frequency, guided by knowledge of the basin evolution or outcrop analogue studies. The utility of outcrop-based studies is immeasurable in areas of production or exploration where datasets are limited. In our study, modelling was conducted after a robust sedimentological, structural, and diagenetic study had established the basin scale and local tectonic controls on facies architecture and distribution, and the timing and style of structurally-related dolomitization and subsequent fracturing. Many studies do not have this luxury, but a careful and thoughtful evaluation of how the tectono-stratigraphic evolution of the basin-controlled sedimentation and fluid flow should allow a series of deterministic scenarios to be modelled within a realistic timeframe. Where there is uncertainty as to which processes have a significant control on reservoir performance, and / or there is limited information on the connectivity of flow controlling bodies, scenario modelling might be effectively captured through experimental design (e.g. Hollis et al., 2011).

There are very few studies that show the importance of capturing geological heterogeneity on fluid flow behaviour in subsurface reservoirs, but where robust geological models have been simulated then the effect on confident prediction of reservoir sweep and recovery efficiency is well demonstrated (e.g. Adams et al., 2011; Hollis et al., 2011). Porosity and permeability in carbonates are closely tied to not only the primary depositional facies but also to diagenetic overprinting and fracturing (Pöppelreiter et al., 2008; Gomes et al., 2018), therefore there is a long-term cost, time and resource benefit to capturing geological heterogeneity as accurately as possible. Process-driven modelling workflows create effective representations of geology within a manageable timeframe. These models will inevitably reduce risk and benefit production forecasting.

6. Conclusions

This principal result of this study is a geologically realistic geocellular model of a carbonate outcrop comprising both depositional and diagenetic geobodies, using a commercial software package. Such a process is important, because many field development plans of subsurface reservoirs require a simple, easy-to-use workflow by which carbonate reservoir architecture can be confidently modelled. A geologically-realistic representation of reservoir architecture is critical to subsequent flow simulation, well planning and investment in capital projects. The creation of such a 3D geocelluar model of an outcrop of the Thebes Formation in the HFF Block has resulted in several outcomes and learnings:

1. The geocelluar models created for this study of the HFF Block accurately reflect the proportion and spatial distribution of complex depositional and diagenetic facies.

2. Two, two-step processes were used to model remobilized slope carbonates in the Thebes Formation. Both methods of facies modelling reflect the volume of remobilised facies in the HFF Block, but object modelling results in a more accurate representation of carbonate mass-transport facies. Both methods overestimated background basinal facies in the upper Thebes Formation, likely due to a lack of “well” control.

3. Probability functions may be used to guide the spatial distribution of structurally-controlled diagenetic geobodies and to associate diagenetic overprinting with facies that have been disproportionately affected by diagenesis (i.e. stratabound dolostones).

4. Multiple stages of diagenesis will result in modification of porosity, permeability, and fracture networks in dolostone bodies that have formed at different times. Dolostones formed over several stages of fault evolution should be characterized and modelled separately to ensure heterogeneity is accurately represented in the model.

5. Modelling steps that represent different stages of the tectonic and platform evolution will result in a more accurate model that may be used for reservoir characterization or exploration purposes.

Acknowledgements

This study was conducted under Industry Technology Facilitator project 3310PSD. The authors would like to thank several generous sponsors for their support of this work: BG Group, Saudi Aramco, Statoil, and Total. We would also like to thank Eagle of the Desert Outfitters and Drs. Richard Newport and Thomas Seers for their assistance in the field. Dr. Enrique Gomez-Rivas and an anonymous reviewer are thanked their suggestions and helpful insights that significantly improved the paper.

References

Adams, E.W., Grélaud, C., Pal, M., Csoma, A.É., Al Ja'aidi, O.S. and Al Hinai, R., 2011. Improving reservoir models of Cretaceous carbonates with digital outcrop modelling (Jabal Madmar, Oman): static modelling and simulating clinoforms. Petroleum Geoscience, 17(3), pp.309-332.

Asmus, J. J. and Grammer, G. M., 2013, Characterization of deepwater carbonate turbidites and mass-transport deposits utilizing high-resolution electrical borehole image logs: Upper Leonardian (Lower Permian) Upper Bone Spring Limestone, Delaware Basin, Southeast New Mexico and West Texas: Gulf Coast Association of Geological Societies Transactions, 63, pp. 27–65.

Balsamo, F., Clemenzi, L., Storti, F., Solum, J. and Taberner, C., 2019. Tectonic control on vein attributes and deformation intensity in fault damage zones affecting Natih platform carbonates, Jabal Qusaybah, North Oman. Journal of Structural Geology, 122, pp.38-57.

Beckert, J., Vandeginste, V. and John, C.M., 2015. Exploring the geological features and processes that control the shape and internal fabrics of late diagenetic dolomite bodies (Lower Khuff equivalent–Central Oman Mountains). Marine and Petroleum Geology, 68, pp.325-340.

Benjakul, R., Hollis, C., Robertson, H.A., Sonnenthal, E.L. and Whitaker, F.F., 2020. Understanding controls on hydrothermal dolomitisation: insights from 3D Reactive Transport Modelling of geothermal convection. Solid Earth Discussions, pp.1-35.

Beucher, H and Renard, D., 2016, Truncated Gaussian and derived methods. Comptes Rendus Geoscience, 348, 510-519

Bisdom, K., Gauthier, B.D.M., Bertotti, G. and Hardebol, N.J., 2014. Calibrating discrete fracture-network models with a carbonate three-dimensional outcrop fracture network: Implications for naturally fractured reservoir modelling. American Association Of Petroleum Geologists bulletin, 98(7), pp.1351-1376.

Bosworth, W., Khalil, S., Clare, A., Comisky, J., Abdelal, H., Reed, T. and Kokkoros, G., 2012. Integration of outcrop and subsurface data during the development of a naturally fractured Eocene carbonate reservoir at the East Ras Budran concession, Gulf of Suez, Egypt. Geological Society London Special Publications, 374(1), pp.333-360.

Bosworth, W., Guiraud, R. and Kessler, L.G., 1999. Late Cretaceous (ca. 84 Ma) compressive deformation of the stable platform of northeast Africa (Egypt): Far-field stress effects of the “Santonian event” and origin of the Syrian arc deformation belt. Geology, 27(7), pp.633-636.

Budd, D.A., Pranter, M.J. and Reza, Z.A., 2006. Lateral periodic variations in the petrophysical and geochemical properties of dolomite. Geology, 34(5), pp.373-376.

Burchette, T.P., 2012. Carbonate rocks and petroleum reservoirs: a geological perspective from the industry. Geological Society London Special Publications, 370(1), pp.17-37.

Burnham, B.S. and Hodgetts, D., 2019. Quantifying spatial and architectural relationships from fluvial outcrops. Geosphere, 15(1), pp.236-253.

Cianfarra, P. and Salvini, F., 2016. Quantification of fracturing within fault damage zones affecting Late Proterozoic carbonates in Svalbard. Rendiconti Lincei, 27(1), pp.229-241.

Corlett, H.J., Bastesen, E., Gawthorpe, R.L., Hirani, J., Hodgetts, D., Hollis, C. and Rotevatn, A., 2018. Origin, dimensions, and distribution of remobilized carbonate deposits in a tectonically active zone, Eocene Thebes Formation, Sinai, Egypt. Sedimentary Geology, 372, pp.44-63.

Deutsch, C.V., Journel, A.G., 1998. GSLIB: Geostatistical Software Library and User’s Guide. 2nd Ed., Oxford University Press, New York.

Eker, A., 2013. Structural analysis of limestones and dolostones within the Hammam Faraun Fault Block, Egypt: Implications for fluid transport and dolomitization. Unpublished Masters Thesis, Department of Earth Science, University of Bergen, Bergen.

Fu, D., Belhaj, H. and Bera, A., 2018. Modeling and simulation of transition zones in tight carbonate reservoirs by incorporation of improved rock typing and hysteresis models. Journal of Petroleum Exploration and Production Technology, 8(4), pp.1051-1068.

Gawthorpe, R.L., Jackson, C.A.L., Young, M.J., Sharp, I.R., Moustafa, A.R. and Leppard, C.W., 2003. Normal fault growth, displacement localisation and the evolution of normal fault populations: the Hammam Faraun fault block, Suez rift, Egypt. Journal of Structural Geology, 25(6), pp.883-895.

Geiger, S and Matthai, S., 2014. What can we learn from high-resolution numerical simulations of single- and multi-phase fluid flow in fractured outcrop analogues. In: Advances in the Study of Fractured Reservoirs (Ed. G. Spence, J. Redfern, R. Guilera, T. Bevan, Cosgrove, J., Couples, G and Daniel, J-M. Geological Society Special Publication, 374, 125-144

Ghadami, N., Rasaei, M.R., Hejri, S., Sajedian, A. and Afsari, K., 2015. Consistent porosity–permeability modeling, reservoir rock typing and hydraulic flow unitization in a giant carbonate reservoir. Journal of Petroleum Science and Engineering, 131, pp.58-69.

Gomes, J., Parra, H. and Ghosh, D., 2018. Quality Control of 3D GeoCellular Models: Examples from UAE Carbonate Reservoirs. In Abu Dhabi International Petroleum Exhibition & Conference. Society of Petroleum Engineers.

Hirani, J., Bastesen, E., Boyce, A., Corlett, H., Gawthorpe, R., Hollis, C., John, C.M., Robertson, H., Rotevatn, A. and Whitaker, F., 2018a. Controls on the formation of stratabound dolostone bodies, Hammam Faraun Fault block, Gulf of Suez. Sedimentology, 65(6), pp.1973-2002.

Hirani, J., Bastesen, E., Boyce, A., Corlett, H., Eker, A., Gawthorpe, R., Hollis, C., Korneva, I. and Rotevatn, A., 2018b. Structural controls on non-fabric selective dolomitization within rift-related basin-bounding normal fault systems: Insights from the Hammam Faraun Fault, Gulf of Suez, Egypt. Basin Research, 30(5), pp.990-1014.

Hollis, C., Price, S., Dijk, H., Wei, L, Frese, D., Van Rijen, M., Al Salhi, M., 2011. Uncertainty management in a giant fractured, carbonate field, Oman. In: ‘Uncertainty Analysis in Reservoir Characterization’ (Ed. Yuan Zee Ma), American Association Of Petroleum Geologists Special Publication, 96, Chapter 9, 137-158.

Hollis, C., Bastesen, E., Boyce, A., Corlett, H., Gawthorpe, R., Hirani, J., Rotevatn, A. and Whitaker, F., 2017. Fault-controlled dolomitization in a rift basin. Geology, 45(3), pp.219-222.

Höntzsch, S., Scheibner, C., Kuss, J., Marzouk, A.M. and Rasser, M.W., 2011. Tectonically driven carbonate ramp evolution at the southern Tethyan shelf: the Lower Eocene succession of the Galala Mountains, Egypt. Facies, 57(1), pp.51-72.

Hubbert, M.K., 1956. Darcy's law and the field equations of the flow of underground fluids. Transactions of the AIME, 207(01), pp.222-239.

Humphrey, E., Gomez-Rivas, E., Neilson, J., Martín-Martín, J.D., Healy, D., Yao, S. and Bons, P.D., 2020. Quantitative analysis of stylolite networks in different platform carbonate facies. Marine and Petroleum Geology, 114, p.104203.

Jackson, C.A.L., Gawthorpe, R.L., Leppard, C.W. and Sharp, I.R., 2006. Rift-initiation development of normal fault blocks: insights from the Hammam Faraun fault block, Suez Rift, Egypt. Journal of the Geological Society, 163(1), pp.165-183.

Janson, X and Madriz, D., 2012. Geomodelling of carbonate mounds using two-point and multipoint statistics. In: Advances in Carbonate Exploration and Reservoir Analysis (Ed. J. Garland, J. Neilson, S. Laubach and K. Whidden). Geological Society of London Special Publication, 370, 229-246.

Jennings, W. J. Jr., 2000. Spatial statistics of permeability data from carbonate outcrops of west Texas and New Mexico: Implications for improved reservoir modeling: Bureau of Economic Geology, University of Texas, Report of Investigations no. 258, 50 p.

Jung, A. and Aigner, T., 2012. Carbonate geobodies: Hierarchical classification and database–a new workflow for 3D reservoir modelling. Journal of Petroleum Geology, 35(1), pp.49-65.

Klimczak, C., Schultz, R.A., Parashar, R. and Reeves, D.M., 2010. Cubic law with aperture-length correlation: implications for network scale fluid flow. Hydrogeology Journal, 18(4), pp.851-862.

Koehrer, B.S., Heymann, C., Prousa, F. and Aigner, T., 2010. Multiple-scale facies and reservoir quality variations within a dolomite body–outcrop analog study from the Middle Triassic, SW German Basin. Marine and Petroleum Geology, 27(2), pp.386-411.

Koeshidayatullah, A., Corlett, H., Stacey, J., Swart, P.K., Boyce, A. and Hollis, C., 2020. Origin and evolution of fault-controlled hydrothermal dolomitization fronts: A new insight. Earth and Planetary Science Letters, 541, p.116291.

Korneva, I., Bastesen, E., Corlett, H., Eker, A., Hirani, J., Hollis, C., Gawthorpe, R.L., Rotevatn, A. and Taylor, R., 2018. The effects of dolomitization on petrophysical properties and fracture distribution within rift-related carbonates (Hammam Faraun Fault Block, Suez Rift, Egypt). Journal of Structural Geology, 108, pp.108-120.

Le Blevec,T., Dubrule, O., John, C. and Hampson, G., 2020. Geostatistical Earth modelling of cyclic depositional facies and diagenesis. American Association of Petroleum Geologists Bulletin, 104, pp. 711-734.

Lapponi, F., Casini, G., Sharp, I., Blendinger, W., Fernández, N., Romaire, I. and Hunt, D., 2011. From outcrop to 3D modelling: a case study of a dolomitized carbonate reservoir, Zagros Mountains, Iran. Petroleum Geoscience, 17(3), pp.283-307.

Ma, D.B., Wu, G.H., Scarselli, N., Luo, X.S., Han, J.F. and Chen, Z.Y., 2019. Seismic damage zone and width–throw scaling along the strike-slip faults in the Ordovician carbonates in the Tarim Basin. Petroleum Science, 16(4), pp.752-762.

Matthäi, S.K., Geiger, S., Roberts, S.G., Paluszny, A., Belayneh, M., Burri, A., Mezentsev, A., Lu, H., Coumou, D., Driesner, T. and Heinrich, C.A., 2007. Numerical simulation of multi-phase fluid flow in structurally complex reservoirs. Geological Society, London, Special Publications, 292(1), pp.405-429.

Mauldon, M. and Dershowitz, W., 2000, November. A multi-dimensional system of fracture abundance measures. In Geological Society of America Abstracts with Programs. 32 (7), p. A474.

Moustafa, A.R. and Abdeen, M.M., 1992. Structural setting of the Hammam Faraun block, eastern side of the Suez rift. Journal-University of Kuwait Science, 19, pp.291-291.

Moustafa, A.R. and Khalil, M.H., 1995. Superposed deformation in the northern Suez Rift, Egypt: relevance to hydrocarbons exploration. Journal of Petroleum Geology, 18(3), pp.245-266.

Patton, T.L., Moustafa, A.R., Nelson, R.A., Abdine, S.A., 1994. Tectonic evolution and structural setting of the Suez Rift. In: Landon, S.M. (Ed.), Interior Rift Basins, vol. 59. American Association of Petroleum Geologists Memoir, pp. 7–55.

Pöppelreiter, M.C., Balzarini, M.A., Hansen, B. and Nelson, R., 2008. Realizing complex carbonate facies, diagenetic and fracture properties with standard reservoir modelling software. Geological Society London Special Publications, 309(1), pp.39-49.

Pranter, M.J., Hirstius, C.B. and Budd, D.A., 2005. Scales of lateral petrophysical heterogeneity in dolomite lithofacies as determined from outcrop analogs: Implications for 3-D reservoir modeling. American Association of Petroleum Geologists Bulletin, 89(5), pp.645-662.

Pyrcz, M.J. and Deutsch, C.V., 2014. Chapter 2 – Modelling Principles. Geostatistical reservoir modelling, 2nd Edition. Oxford university press. p.27-40.

Robson, D.A., 1971. The structure of the Gulf of Suez (clysmic) rift, with special references to the eastern side. Journal of the Geological Society of London 127, 247–267.

Saller, A.H. and Henderson, N., 1998. Distribution of porosity and permeability in plat- form dolomites: insight from the Permian of West Texas. American Association of Petroleum Geologists Bulletin, 82 (8), pp. 1528–1550.

Scheibner, C., Reijmer, J.J.G., Marzouk, A.M., Speijer, R.P. and Kuss, J., 2003. From platform to basin: the evolution of a Paleocene carbonate margin (Eastern Desert, Egypt). International Journal of Earth Sciences, 92(4), pp.624-640.

Schütz, K. I., 1994, Structure and stratigraphy of the Gulf of Suez, Egypt, in S. M. Landon, ed., Interior rift basins: American Association Of Petroleum Geologists Memoir 59, p. 57–96

Sharp, I.R., Gawthorpe, R.L., Underhill, J.R. and Gupta, S., 2000. Fault-propagation folding in extensional settings: Examples of structural style and synrift sedimentary response from the Suez rift, Sinai, Egypt. Geological Society of America Bulletin, 112(12), pp.1877-1899.

Sharp, I.R., Gillespie, P., Horn, S., Lonoy, A. and Morsalnezhad, D., 2006. January. Outcrop characterisation of fractured Cretaceous carbonate reservoirs, Zagros Mts, Iran. In International Oil Conference and Exhibition in Mexico. Society of Petroleum Engineers. SPE 10400.

Sharp, I., Gillespie, P., Morsalnezhad, D., Taberner, C., Karpuz, R., Vergés, J., Horbury, A., Pickard, N., Garland, J. and Hunt, D., 2010. Stratigraphic architecture and fracture-controlled dolomitization of the Cretaceous Khami and Bangestan groups: an outcrop case study, Zagros Mountains, Iran. Geological Society London Special Publications, 329(1), pp.343-396.

Skalinski, M. and Kenter, J.A., 2015. Carbonate petrophysical rock typing: integrating geological attributes and petrophysical properties while linking with dynamic behaviour. Geological Society, London, Special Publications, 406(1), pp.229-259.

Spence, G.H. and Finch, E., 2014. Influences of nodular chert rhythmites on natural fracture networks in carbonates: an outcrop and two-dimensional discrete element modelling study. Geological Society London Special Publications, 374(1), pp.211-249.

Wang X (2005) Stereological interpretation of rock fracture traces on borehole walls and other cylindrical surfaces. PhD Thesis, Virginia Polytechnic Institute and State, Blacksburg, VA, USA.

Watanabe, N., Kusanagi, H., Shimazu, T. and Yagi, M., 2019. Local non-vuggy modeling and relations among porosity, permeability and preferential flow for vuggy carbonates. Engineering Geology, 248, pp.197-206.

Warden, A., 2014. Petrophysical, fracture modelling and simulation of a fractured carbonate outcrop: Hammam Faraun Fault Block, Sinai Peninsula, Gulf of Suez, Egypt. Unpublished MEng Thesis, University of Manchester

Warrlich, G.M., Amthor, J., Abu-shiekah, I.M., Al-Kharusi, A.S., Al-Kindy, M.H. and Garimella, S.V., 2011, January. Adjusting modeling methodologies to decision requirements, reservoir properties and recovery mechanism-examples from the Shuaiba in Oman. In SPE Reservoir Characterisation and Simulation Conference and Exhibition. Society of Petroleum Engineers.

Yapparova, A., Gabellone, T., Whitaker, F., Kulik, D.A. and Matthäi, S.K., 2017. Reactive transport modelling of hydrothermal dolomitisation using the CSMP++ GEM coupled code: Effects of temperature and geological heterogeneity. Chemical Geology, 466, pp.562-574.

Yao, S., Gomez-Rivas, E., Martin-Martin, J.D., Gómez-Gras, D., Travé, A., Griera, A., Howell, J. and Qing, H., 2020. Fault-controlled dolostone geometries in a transgressive-regressive sequence stratigraphic framework. Sedimentology, 67(6), pp.3290-3316.

Young, M.J., Gawthorpe, R.L. and Sharp, I.R., 2003. Normal fault growth and early syn-rift sedimentology and sequence stratigraphy: Thal Fault, Suez Rift, Egypt. Basin Research, 15(4), pp.479-502.

Youssef, M.M., 2003. Structural setting of central and south Egypt: an overview. Micropaleontology, 49, pp.1-13.

Zeeb, C., Gomez-Rivas, E., Bons, P.D. and Blum, P., 2013. Evaluation of sampling methods for fracture network characterization using outcrops. American Association of Petroleum Geologists Bulletin, 97(9), pp.1545-1566.

Fig. 1. Location map (inset) and stratigraphy of the study area. The Thebes Formation facies are differentiated in the larger map.

Fig. 2. A) Location of sedimentary and laser logs used in the model (Google Earth V.E. 3x); B) i – Gebel Fault, ii – Gebel Fault branch, iii - Hammam Faraun Fault, iv – Thal Fault; and C) basic stratigraphic model.

Fig. 3. Two methods of facies modelling and resultant lower and upper Thebes facies models.

Fig. 4. A) Field photo of R-1 debrite (outlined); and B) facies B-1 and R-5 in the upper Thebes Fm. Facies R-5 are found at the top of 20-30m thick B-1 basinal wackestones. C) A crossplot showing the horizontal distance, along depositional dip versus thickness of the R-1 versus R-5 facies and the R-1 geobodies, both parallel and perpendicular to depositional strike (inset). These measurements were calibrated with a laser range finder in the field.

Fig. 5. Dolostone 'facies' overprint workflow. A) Stratabound dolostone probability. B) Non-stratabound dolostone probability. C) IF statement restricting dolostone to facies R-1. D) Combination of probability modelling and IF statement. E) Introduction of smooth random function. F) Final probability model for Hypothesis A.

Fig. 6. Probability modelling for Hypothesis B non-stratabound dolostone. A) Fault sticks used to model probability of dolostone occurring up to 500 meters from the fault sticks. Fault sticks represent a possible fluid pathway for dolomitizing fluid associated with the HF fault. B) Stratabound dolostone associated with non-stratabound dolostone in facies R-1. C) Combined non-stratabound and stratabound dolostone associated with non-stratabound dolostone probability model. D) Results of modelling Hypothesis B (see Figure 3 for thee facies legend).

Fig. 7. Fisher K distribution factor, mean dip and azimuth and P_{32} for all fractures within principal facies in the Thebes Formation.

Fig. 8. Fisher K distribution factor, mean dip and azimuth and P_{32} for all fractures within the dolostone bodies.

Fig. 9. Plan view of a scanline with each fracture representing a different fracture set. All fractures are equally spaced. The scanline intersects all fractures of the blue fracture set so P10=P32 and C31=1 as □=0^{o}. The scanline only intersects 4 fractures of the green set, so the apparent intensity is inaccurate, and requires a correction of C31=1.5 giving the correct intensity of 6m^{-1}. The red fracture set is not intersected so C31= infinity.

Fig. 10. A) and B) comparison of facies model for the HFF Block and fracture intensity. The highest fracture densities are modelled within the non-stratabound dolostone (37.5m^{-1}), in the core of the HFF, and within the thin-bedded wackestone facies (also ~37m^{-1}), consistent with field observations. Stratabound dolostone bodies have an average intensity of 32m^{-1} and packstones 22m^{-1}, with the grainstones and conglomeratic facies exhibiting the lowest intensities (17.m^{-1}), also consistent with field observations. C) and D) average fracture dip and azimuth for fractures in the HFF Block. The majority of fractures are steeply dipping (50-80^{o}). Fracture orientations largely parallel the Gebel Fault, reflecting the dominance of

scanlines in this locality. However, the non-stratabound dolostone bodies show a different azimuth, reflecting the trend of the HFF.

Fig. 11. Discrete Fracture Network model of the HFF Block.

Fig. 12. Fracture permeability for the IFM (A) and DFN (B), non-stratabound dolostone body only. Since the same fracture aperture was used throughout, the values are mostly ~474,960mD with variation resulting from the outlying 'tail' of the log normal distribution.

Fig. 13. A) Qualitative assessment of two facies modelling methods compared to field photos; and B) Quantitative comparison of well log input, upscaling, and modelled facies (SIS and Object Modelling).

Fig. 14. Result of modelling Hypothesis A and Hypothesis B.

Fig. 15. A) Porosity (m^3/m^3) model for the HFF Block. Note the northward increase in porosity associated with the highly microporous Basinal wackestone and mudstone (Facies B-1) of the upper Thebes Formation; B) Permeability (mD) model for the HFF Block.

Figure 1

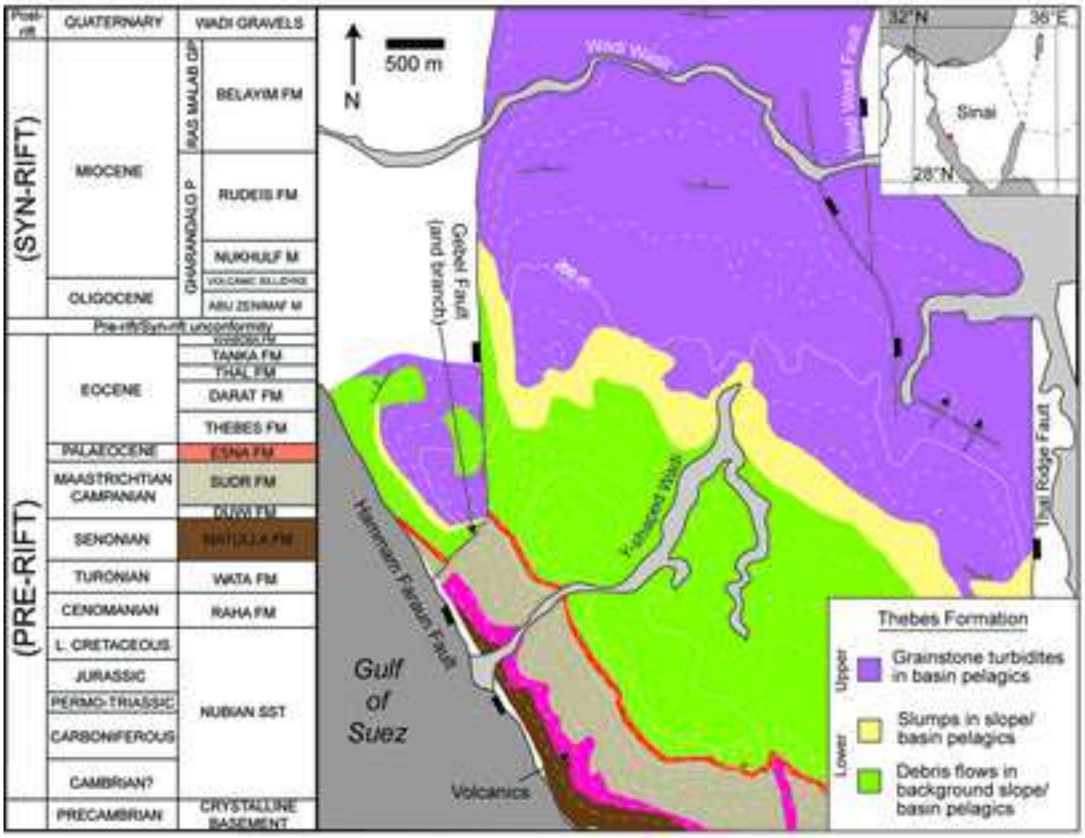
Post-rift
QUATERNARY
WADI GRAVELS
(SYN-RIFT)
MIOCENE
RAS MALAB GP
BELAYIM FM
GHARANDAL G P
RUDEIS FM
NUKHUL F M
ABU ZENIMA F M
OLIGOCENE
Pre-rift/Syn-rift unconformity
(PRE-RIFT)
EOCENE
TANKA FM
THAL FM
DARAT FM
THEBES FM
PALAEOCENE
ESNA FM
MAASTRICHTIAN CAMPANIAN
SUDR FM
DUWI FM
SENONIAN
MATULLA FM
TURONIAN
WATA FM
CENOMANIAN
RAHA FM
L. CRETACEOUS
JURASSIC
PERMO-TRIASSIC
CARBONIFEROUS
NUBIAN SST
CAMBRIAN?
PRECAMBRIAN
CRYSTALLINE BASEMENT
N
500 m
Wadi Wasit
Wadi Wasit Fault
Gebel Fault (and branch)
Y-shaped Wadi
Hammam Faraun Fault
Gulf of Suez
Volcanics
Thal Ridge Fault
32°N
36°E
Sinai
28°N
Thebes Formation
Upper
Lower
Grainstone turbidites in basin pelagics
Slumps in slope/ basin pelagics
Debris flows in background slope/ basin pelagics

Figure 2

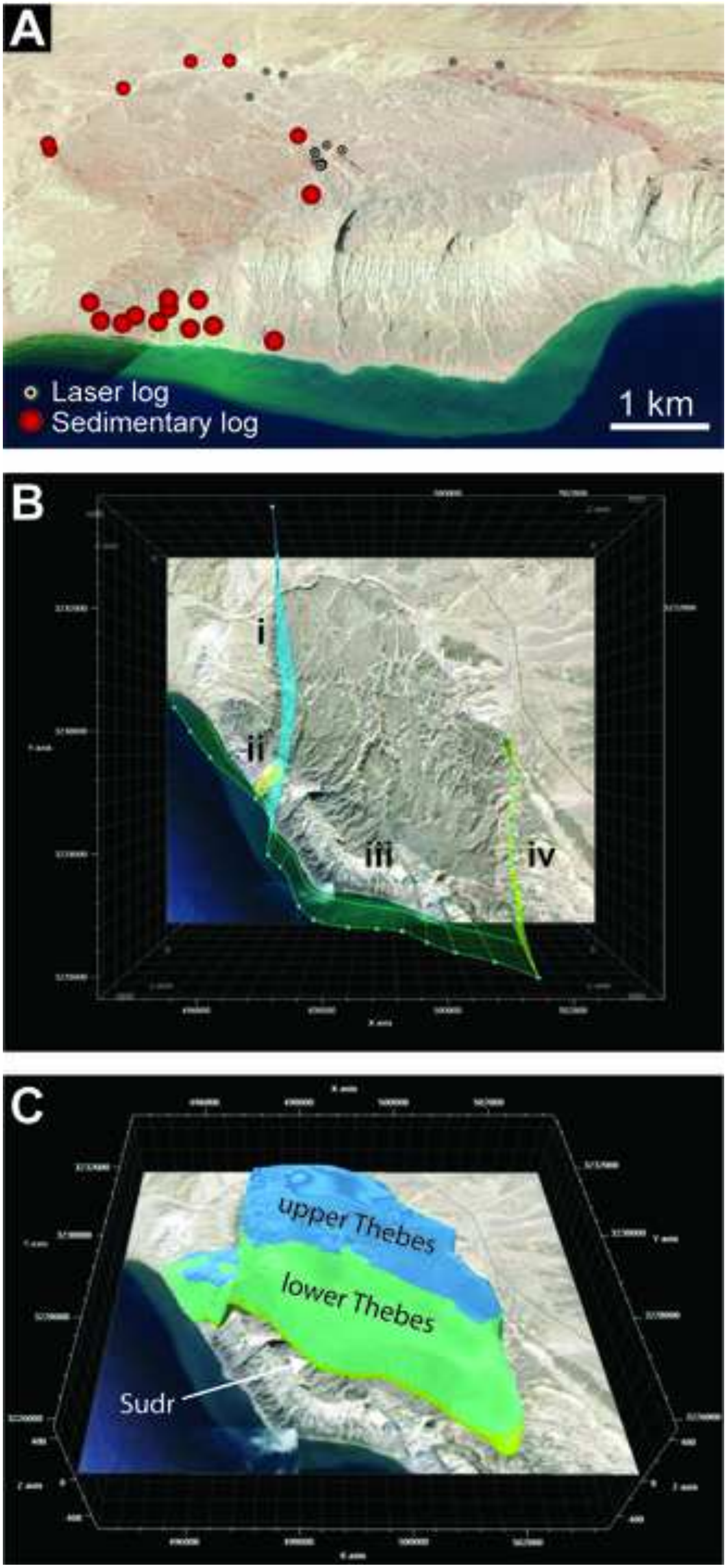
A
○ Laser log
● Sedimentary log
1 km
B
i
ii
iii
iv
C
upper Thebes
lower Thebes
Sudr

Figure 3

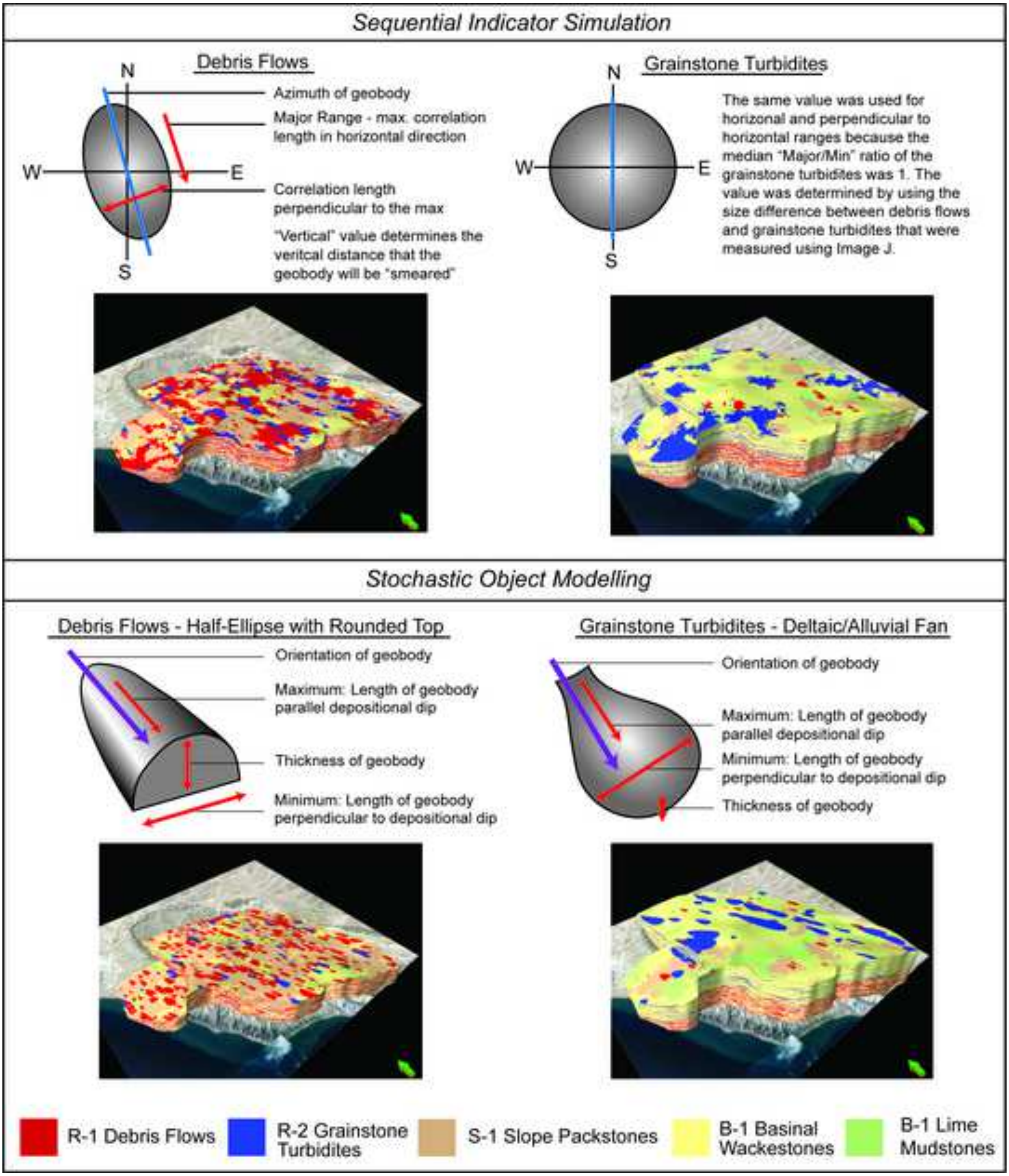

Sequential Indicator Simulation

Debris Flows

Azimuth of geobody

Major Range - max. correlation length in horizontal direction

Correlation length perpendicular to the max

"Vertical" value determines the veritcal distance that the geobody will be "smeared"

Grainstone Turbidites

The same value was used for horizonal and perpendicular to horizontal ranges because the median "Major/Min" ratio of the grainstone turbidites was 1. The value was determined by using the size difference between debris flows and grainstone turbidites that were measured using Image J.

Stochastic Object Modelling

Debris Flows - Half-Ellipse with Rounded Top

Orientation of geobody

Maximum: Length of geobody parallel depositional dip

Thickness of geobody

Minimum: Length of geobody perpendicular to depositional dip

Grainstone Turbidites - Deltaic/Alluvial Fan

Orientation of geobody

Maximum: Length of geobody parallel depositional dip

Minimum: Length of geobody perpendicular to depositional dip

Thickness of geobody

🟥 R-1 Debris Flows
🟦 R-2 Grainstone Turbidites
🟫 S-1 Slope Packstones
🟨 B-1 Basinal Wackestones
🟩 B-1 Lime Mudstones

Figure 4

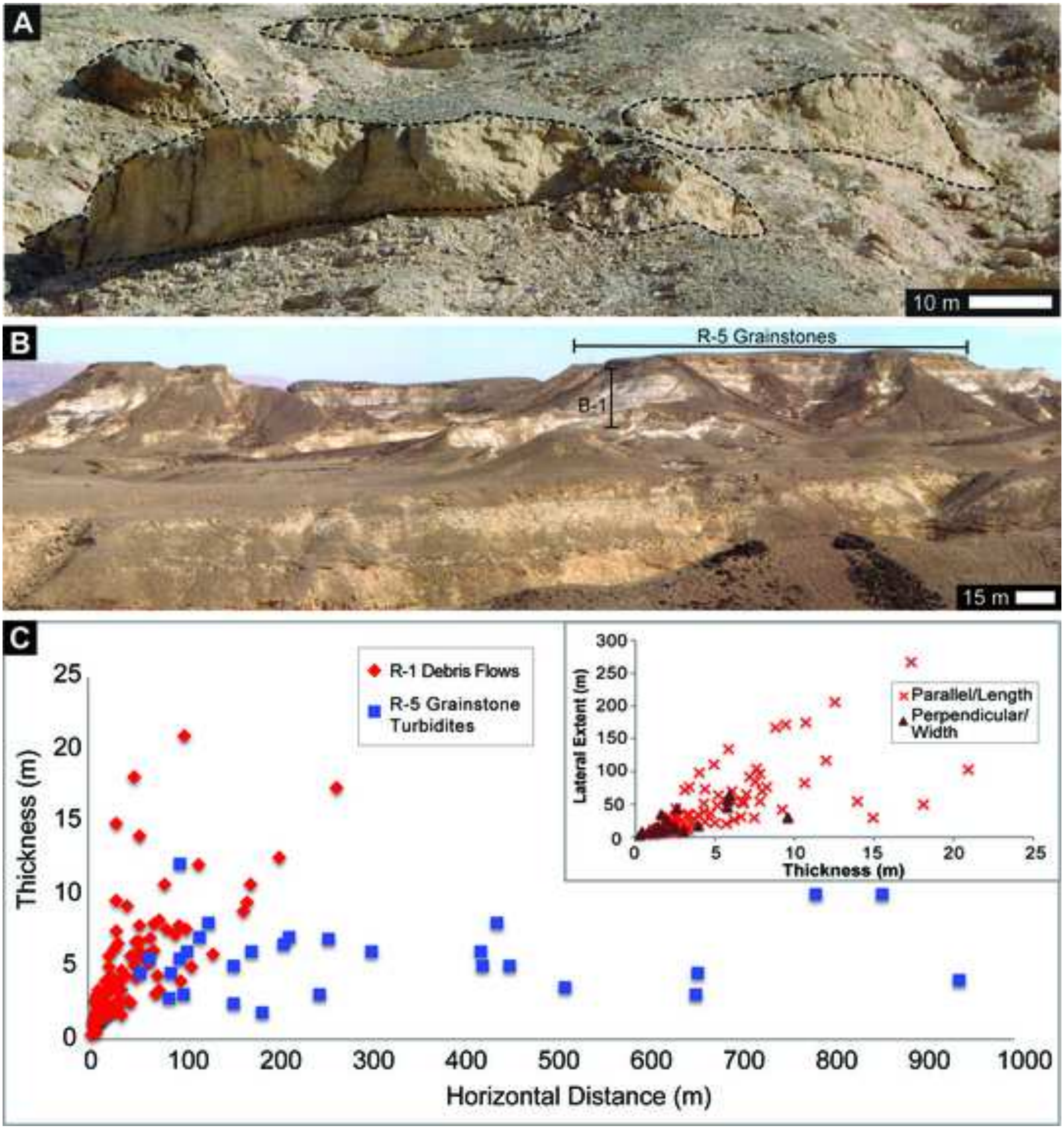
A
10 m
B
R-5 Grainstones
B-1
15 m
C
Thickness (m)
25
20
15
10
5
0
0
100
200
300
400
500
600
700
800
900
1000
Horizontal Distance (m)
R-1 Debris Flows
R-5 Grainstone Turbidites
Lateral Extent (m)
300
250
200
150
100
50
0
0
5
10
15
20
25
Thickness (m)
Parallel/Length
Perpendicular/ Width

Figure 5

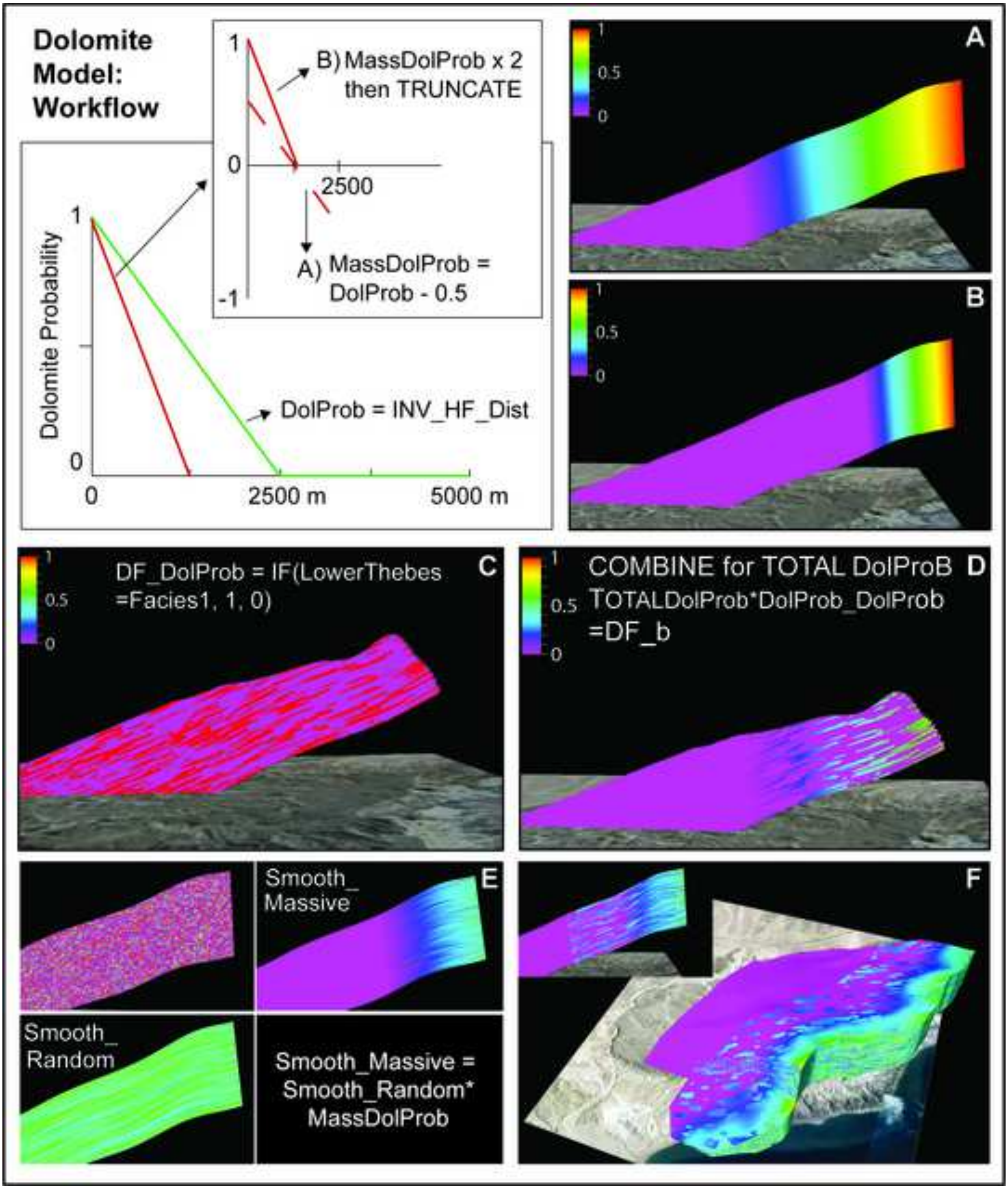
Dolomite Model: Workflow
1
B) MassDolProb x 2 then TRUNCATE
0
2500
A) MassDolProb = DolProb - 0.5
-1
Dolomite Probability
1
0
DolProb = INV_HF_Dist
0
2500 m
5000 m
A
1
0.5
0
B
1
0.5
0
C
DF_DolProb = IF(LowerThebes =Facies1, 1, 0)
1
0.5
0
D
COMBINE for TOTAL DolProB
TOTALDolProb*DolProb_DolProb =DF_b
1
0.5
0
E
Smooth_ Massive
Smooth_ Random
Smooth_Massive = Smooth_Random* MassDolProb
F

Figure 6

Click here to download high resolution image

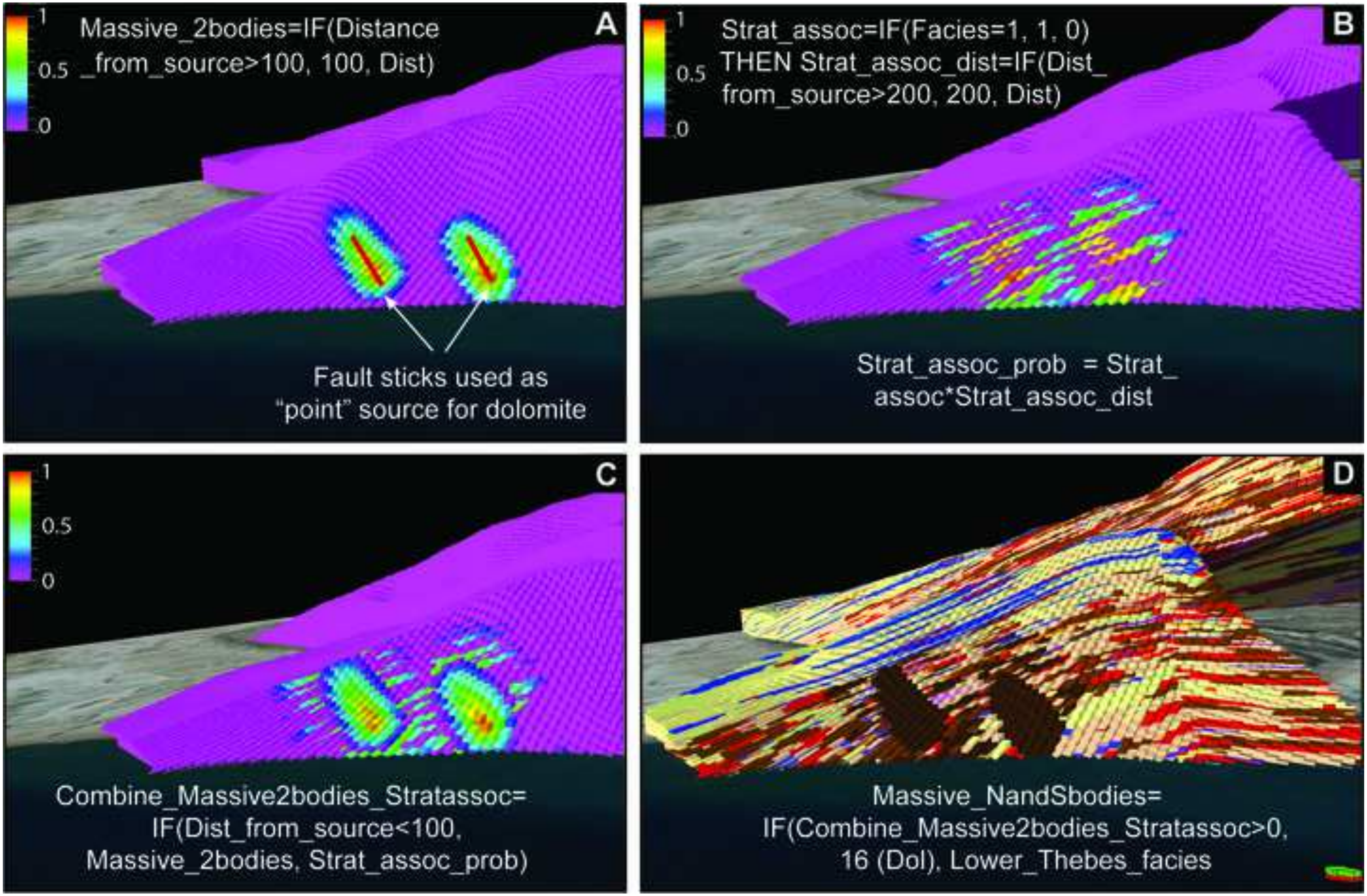

Figure 7

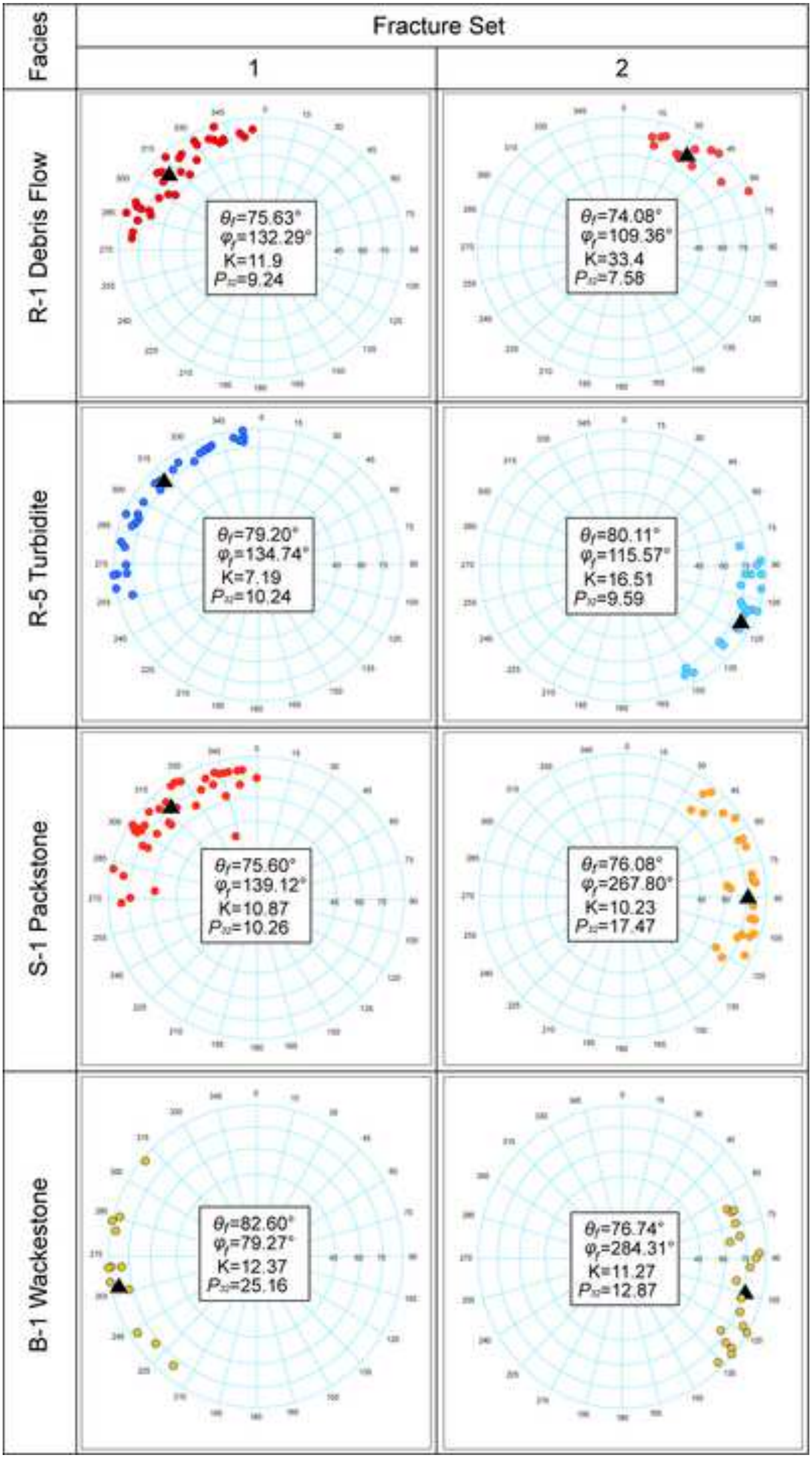
Facies
Fracture Set
1
2
R-1 Debris Flow
θf=75.63°
φf=132.29°
K=11.9
P32=9.24
θf=74.08°
φf=109.36°
K=33.4
P32=7.58
R-5 Turbidite
θf=79.20°
φf=134.74°
K=7.19
P32=10.24
θf=80.11°
φf=115.57°
K=16.51
P32=9.59
S-1 Packstone
θf=75.60°
φf=139.12°
K=10.87
P32=10.26
θf=76.08°
φf=267.80°
K=10.23
P32=17.47
B-1 Wackestone
θf=82.60°
φf=79.27°
K=12.37
P32=25.16
θf=76.74°
φf=284.31°
K=11.27
P32=12.87

Figure 8

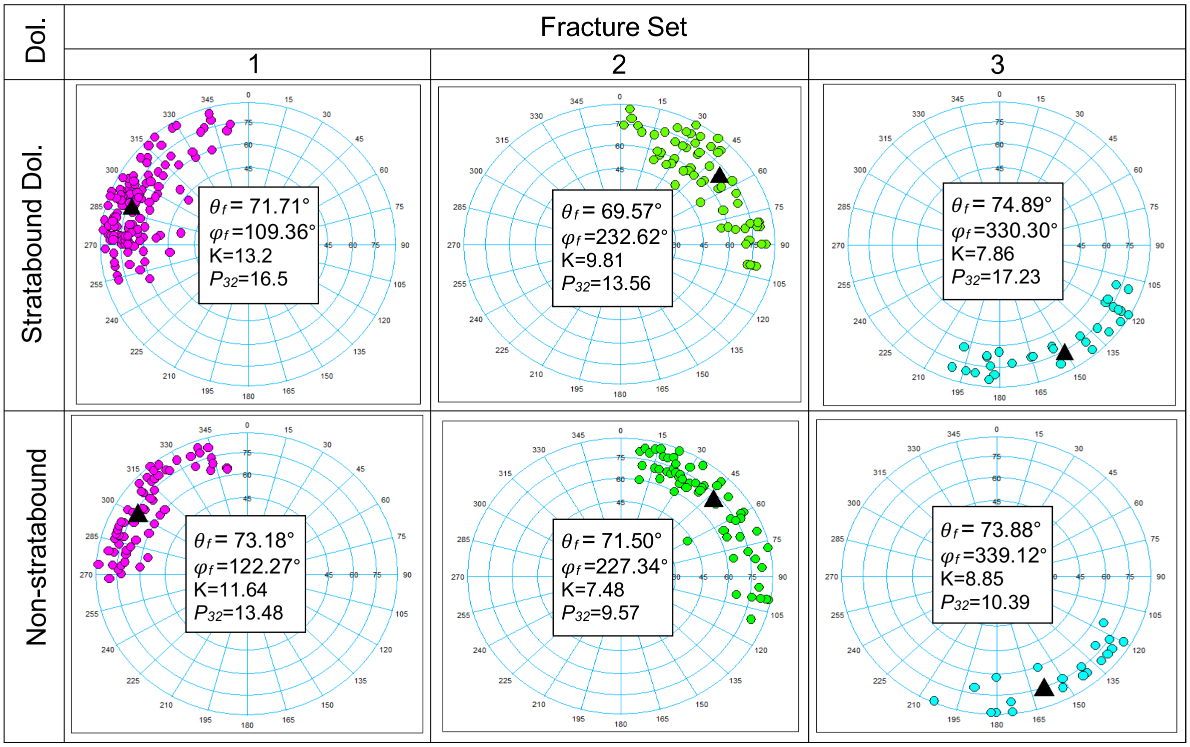

Dol.
Fracture Set
1
2
3
Stratabound Dol.
θ_f= 71.71°
φ_f=109.36°
K=13.2
P_{32}=16.5
θ_f= 69.57°
φ_f=232.62°
K=9.81
P_{32}=13.56
θ_f= 74.89°
φ_f=330.30°
K=7.86
P_{32}=17.23
Non-stratabound
θ_f= 73.18°
φ_f=122.27°
K=11.64
P_{32}=13.48
θ_f= 71.50°
φ_f=227.34°
K=7.48
P_{32}=9.57
θ_f= 73.88°
φ_f=339.12°
K=8.85
P_{32}=10.39
0
15
30
45
60
75
90
105
120
135
150
165
180
195
210
225
240
255
270
285
300
315
330
345

Figure 9

Click here to download high resolution image

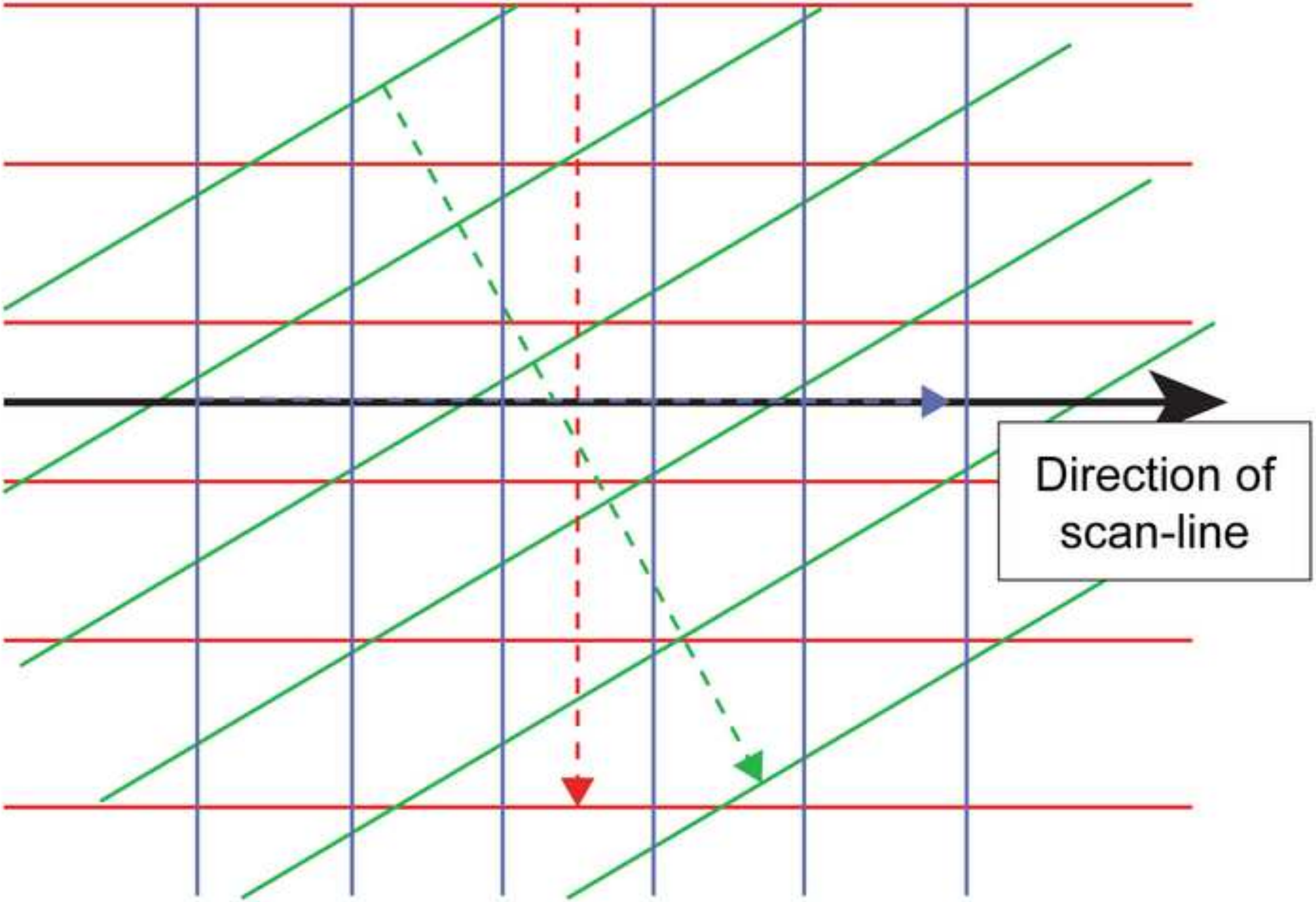

Figure 10

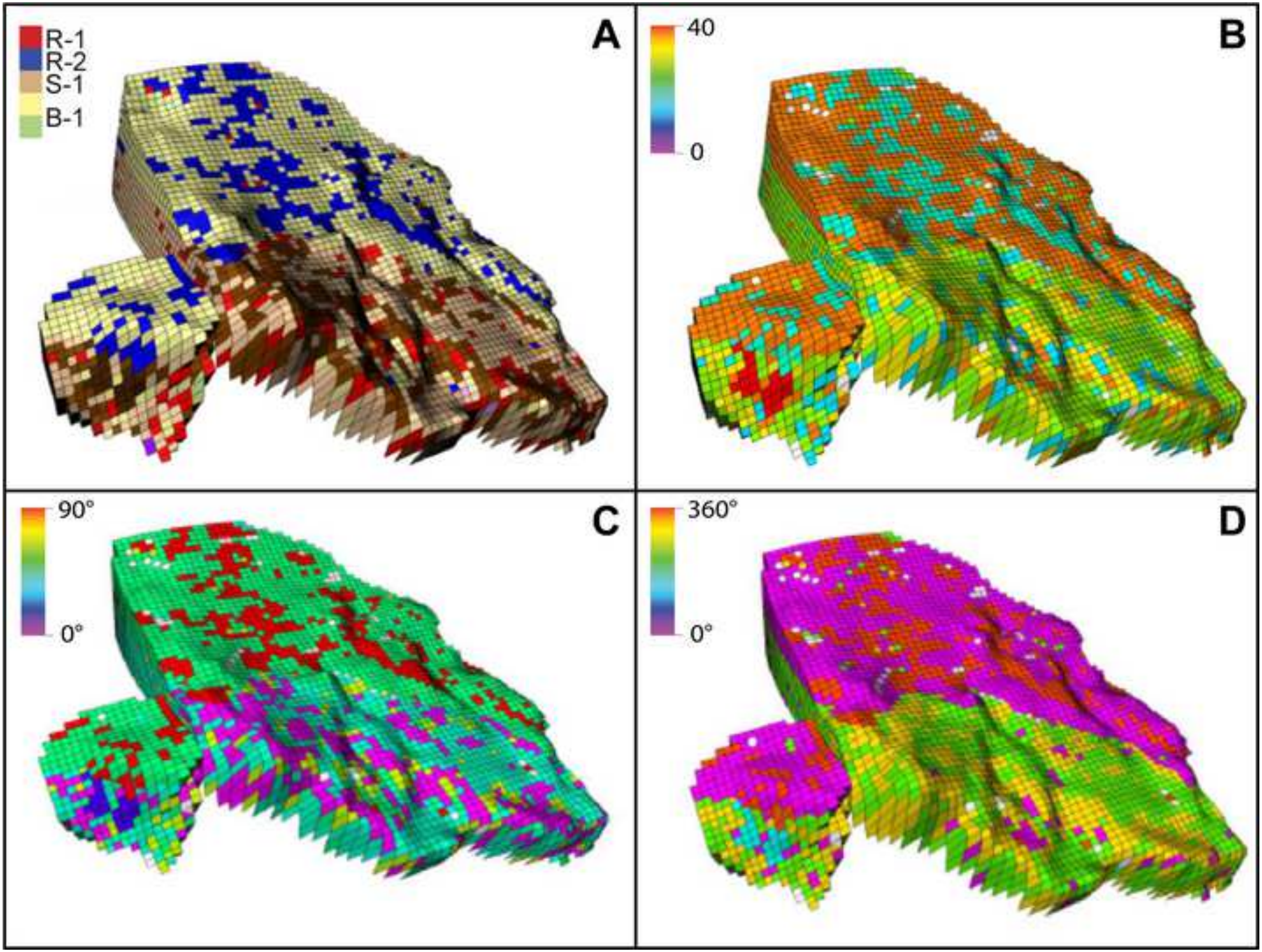

Figure 11

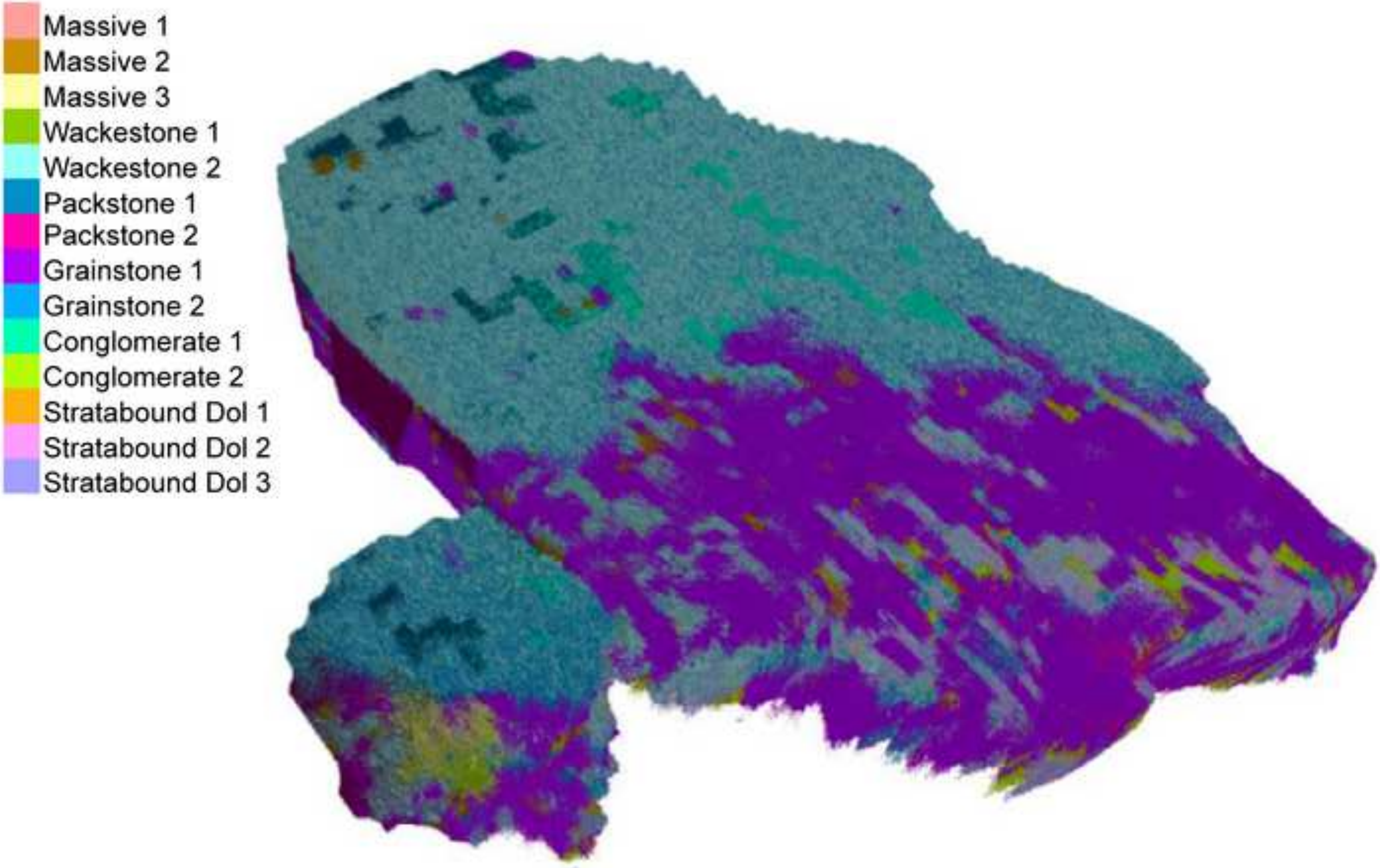
Massive 1
Massive 2
Massive 3
Wackestone 1
Wackestone 2
Packstone 1
Packstone 2
Grainstone 1
Grainstone 2
Conglomerate 1
Conglomerate 2
Stratabound Dol 1
Stratabound Dol 2
Stratabound Dol 3

Figure 13

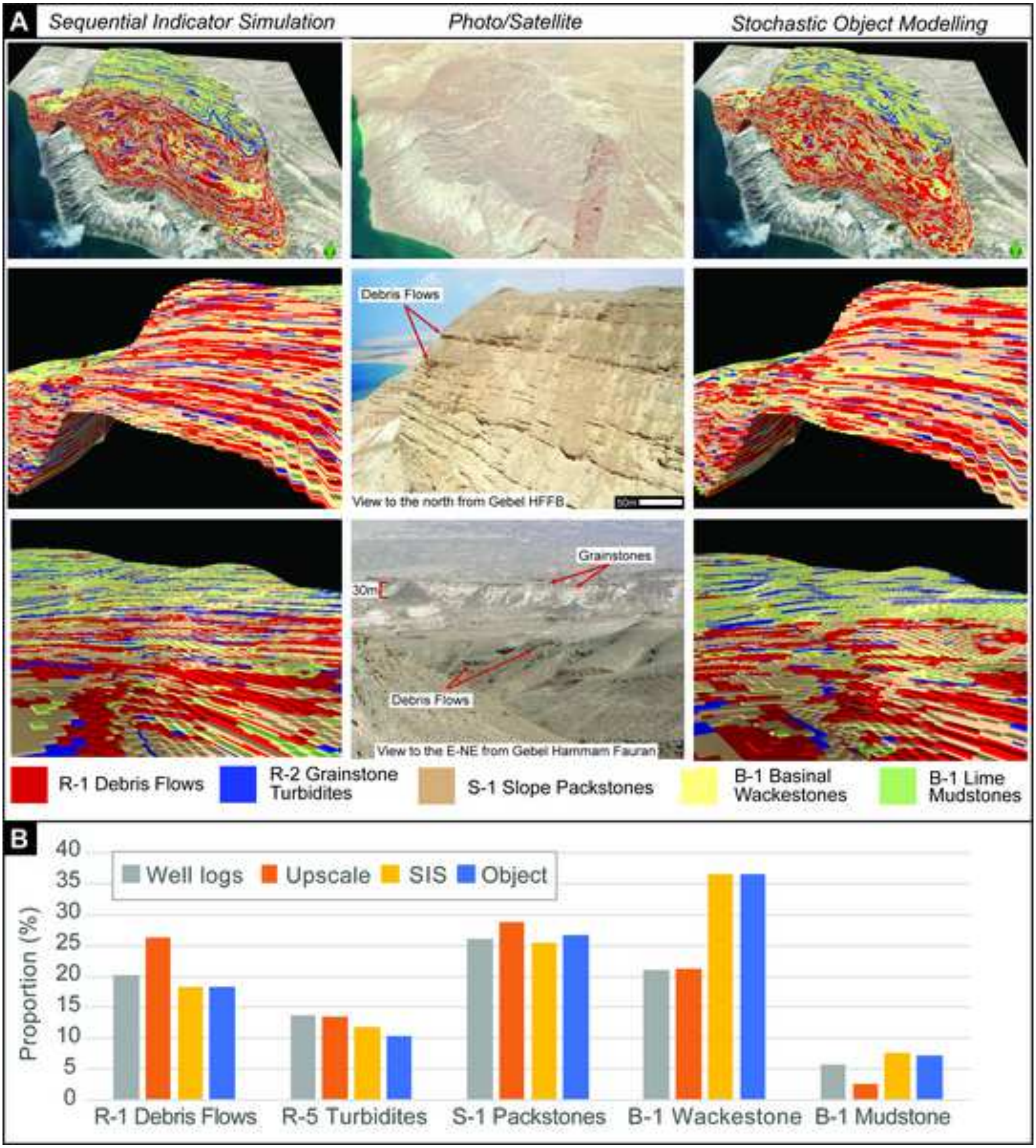
A
Sequential Indicator Simulation
Photo/Satellite
Stochastic Object Modelling
Debris Flows
View to the north from Gebel HFFB
50m
Grainstones
30m
Debris Flows
View to the E-NE from Gebel Hammam Fauran
🟥 R-1 Debris Flows
🟦 R-2 Grainstone Turbidites
S-1 Slope Packstones
B-1 Basinal Wackestones
🟩 B-1 Lime Mudstones
B
Well logs
Upscale
SIS
Object
Proportion (%)
40
35
30
25
20
15
10
5
0
R-1 Debris Flows
R-5 Turbidites
S-1 Packstones
B-1 Wackestone
B-1 Mudstone

Figure 12

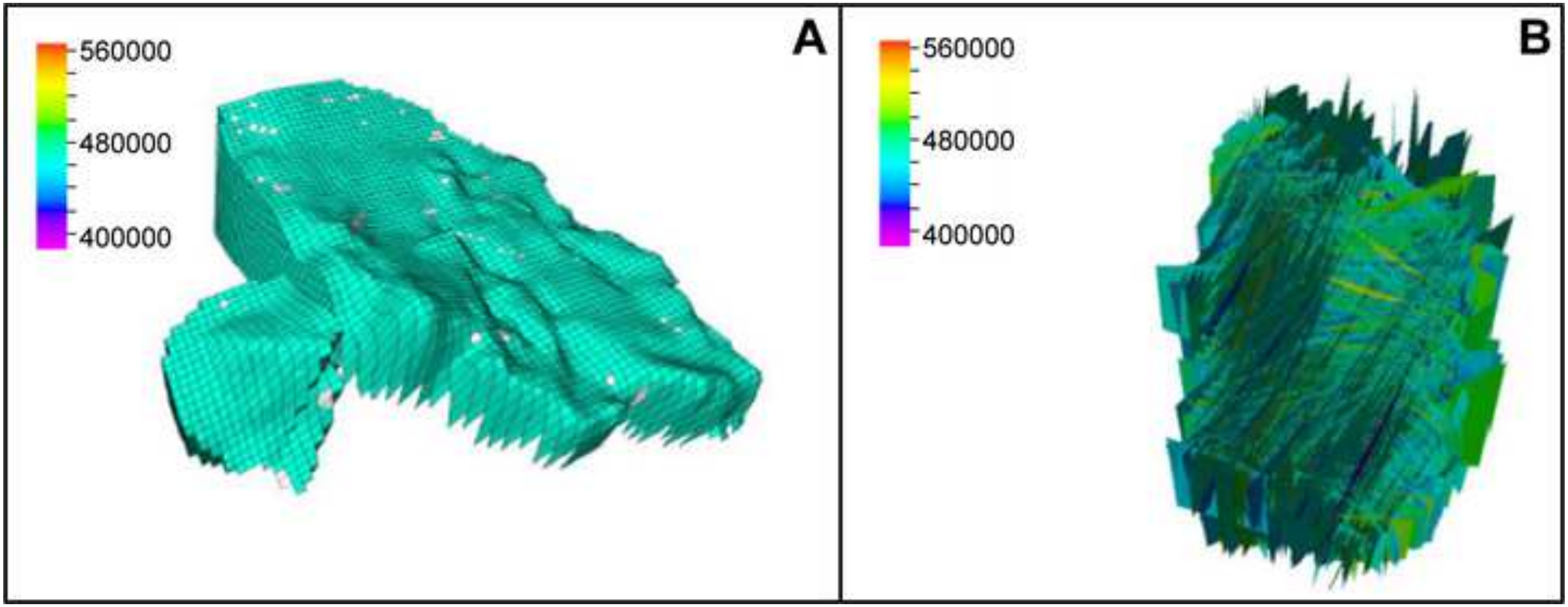

Figure 14

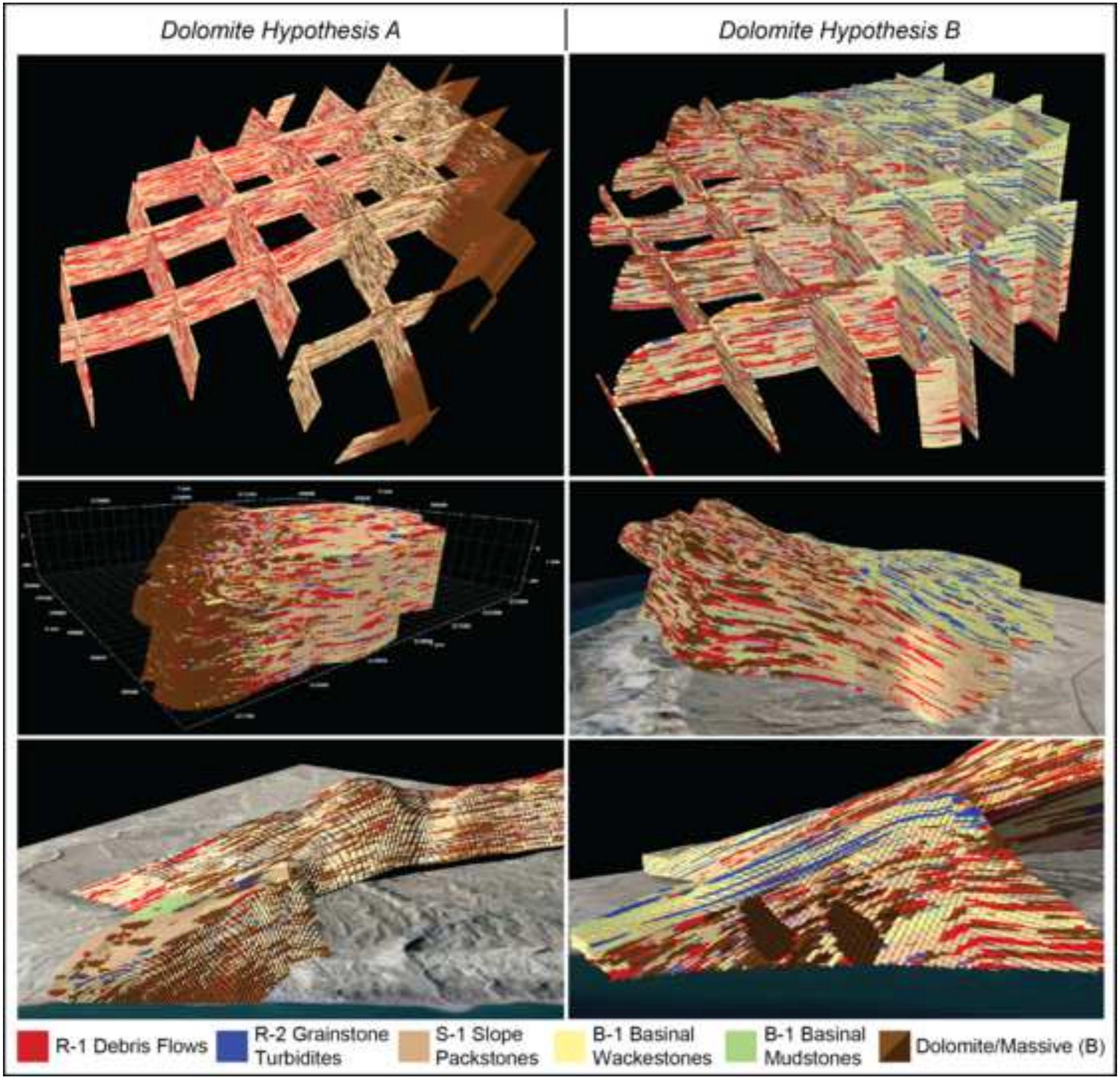
Dolomite Hypothesis A
Dolomite Hypothesis B
R-1 Debris Flows
R-2 Grainstone Turbidites
S-1 Slope Packstones
B-1 Basinal Wackestones
B-1 Basinal Mudstones
Dolomite/Massive (B)

Figure 15

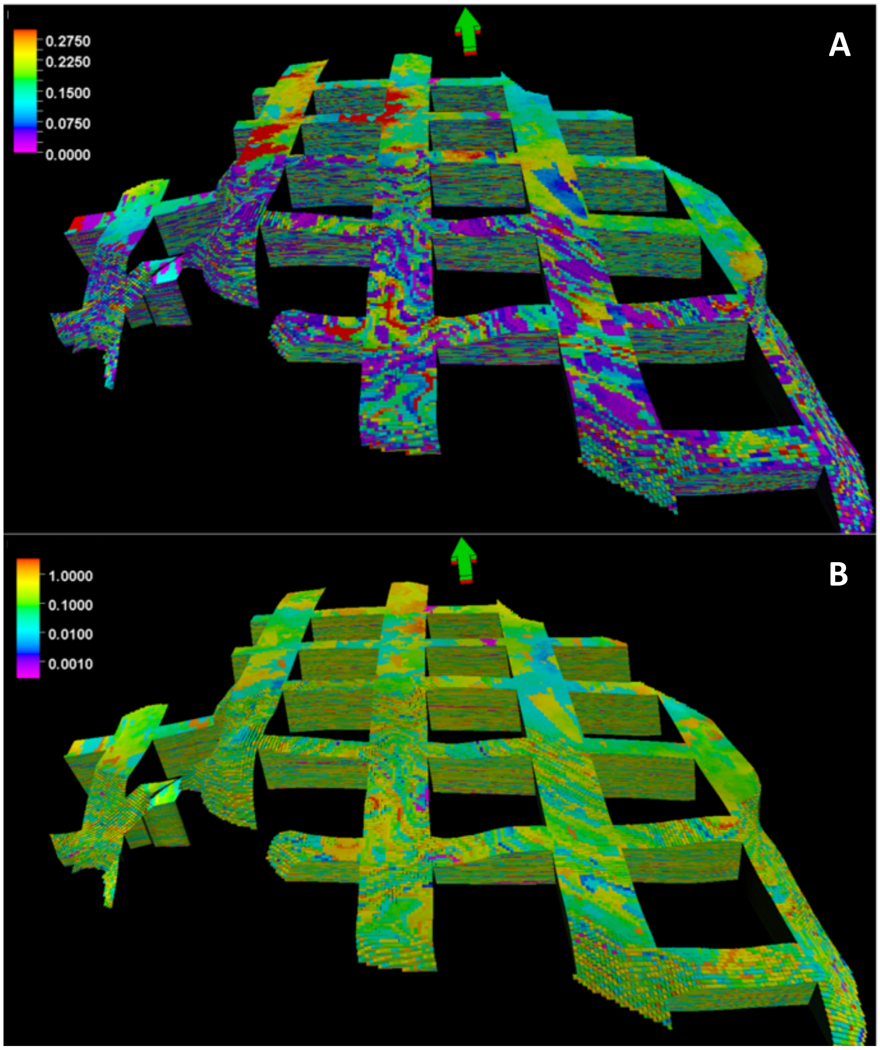

Table 1

Facies	**Geobody shape and contacts**	**Dimensions**	**Field Photo**	**Interpretation** (see Corlett et al. 2018 for more detailed interpretations)
R-1: Matrix-rich debrite	Lens-shaped; irregular basal contact, concave upper contact	Down-dip length: 3-267 m Along-strike length: 2-64 m Thickness: 0.3-20 m		Viscous debrite
R-2: Graded grainstone turbidite	Sheet-like: sharp irregular basal contact, flat upper contact	Down-dip length: 2-50 m Along-strike length: up to 100 m Thickness: 0.5-6 m	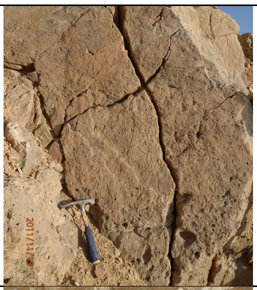	Turbidite flow
R-3: Matrix-free debris sheet flow	Sheet-like: scoured base, sharp flat upper contact	Down-dip length: up to 1000 m, Along-strike length: up to 1500 m Thickness: 0.3-2 m		Collapse debris sheet flow
R-4: Slumped grainstone	Lens-shaped bodies; sharp upper and lower convex contact	Down-dip length: 1-5 m, Along-strike length: up to 10 m Thickness: 1-3 m		Plastic flow slump
R-5: High-density turbidite grainstone	Sheet-like; sharp, flat upper and lower contact	Down-dip length and along-strike length: between 57-940 m Thickness: 0.5-10 m		High density turbidite flow
R-6: Channelized grainstone	Lens-shaped; scoured base, convex upper contact	Down-dip length: unknown Along-strike: 3-5 m Thickness: 8-20 m		Channelized flow

Table 1. Remobilized facies in the Thebes Formation at HFF BLOCK (modified from Corlett et al., 2018).

Facies	**Max Bed Thickness**	**Maximum Fracture Length**
Conglomerate	49.3m	98.6m
Packstone	68.3m	136.4m
Wackestone	39.7m	79.4m
Grainstone	34.1m	68.2m
Stratabound dolostone	49.3m	98.6m
Non-stratabound Dolostone	157.2m	314.4m

Table 2. Maximum fracture length per facies.

Table 3

Porosity (frac.)					
	Minimum	Maximum	Mean	Std	Variance
Data	0.00	0.39	0.10	0.08	0.01
Model	0.00	0.39	0.18	0.08	0.01
Permeability (md)					
	Minimum	Maximum	Mean	Std	Variance
Data	0.00	3.49	0.37	0.67	0.45
Model	0.00	3.49	0.72	0.65	0.42

Table 3. Comparison of average, range, standard deviation and variance of modelled porosity and permeability, compared to input data.

***Credit Author Statement**

Hilary Corlett: Writing – Original draft preparation, Reviewing, and Editing; Conceptualization, Methodology, Data Collection, Modelling, Fieldwork **David Hodgetts**: Methodology, Modelling, Fieldwork **Jesal Hirani**: Fieldwork, Methodology, Data Collection **Atle Rotevatn**: Fieldwork, Methodology, Data Collection and Curation **Rochelle Taylor**: Methodology, Data Collection and Curation, Writing - Editing **Cathy Hollis:** Conceptualization, Writing – Original draft preparation, Reviewing, and Editing